

# Hybrid metal-semiconductor quantum dots in InAs as a platform for quantum simulation

Praveen Sriram\* and Connie L. Hsueh\*

*Department of Applied Physics, Stanford University, Stanford CA 94305, USA  
Stanford Institute for Materials and Energy Sciences, SLAC National Accelerator Laboratory, Menlo Park, California 94025, USA and  
Geballe Laboratory for Advanced Materials, Stanford University, Stanford, California 94305, USA*

Karna Morey

*Geballe Laboratory for Advanced Materials, Stanford University, Stanford, California 94305, USA and  
Department of Physics, Stanford University, Stanford CA 94305, USA*

Tiantian Wang and Candice Thomas

*Department of Physics and Astronomy, Purdue University, West Lafayette, Indiana 47907, USA and  
Birck Nanotechnology Center, West Lafayette, Indiana 47907, USA*

Geoffrey C. Gardner

*Birck Nanotechnology Center, Purdue University, West Lafayette, Indiana 47907, USA and  
Microsoft Quantum Lab West Lafayette, West Lafayette, Indiana 47907, USA*

Marc A. Kastner

*Stanford Institute for Materials and Energy Sciences, SLAC National Accelerator Laboratory, Menlo Park, California 94025, USA  
Department of Physics, Massachusetts Institute of Technology, Cambridge, MA 02139, USA and  
Department of Physics, Stanford University, Stanford CA 94305, USA*

Michael J. Manfra

*Department of Physics and Astronomy, Purdue University, West Lafayette, Indiana 47907, USA  
Elmore Family School of Electrical and Computer Engineering,  
Purdue University, West Lafayette, Indiana 47907, USA  
School of Materials Engineering, Purdue University, West Lafayette, Indiana 47907, USA  
Birck Nanotechnology Center, West Lafayette, Indiana 47907, USA and  
Microsoft Quantum Lab West Lafayette, West Lafayette, Indiana 47907, USA*

David Goldhaber-Gordon

*Stanford Institute for Materials and Energy Sciences, SLAC National Accelerator Laboratory, Menlo Park, California 94025, USA and  
Department of Physics, Stanford University, Stanford CA 94305, USA  
(\*goldhaber-gordon@stanford.edu)  
(Dated: August 7, 2025)*

Arrays of hybrid metal-semiconductor islands offer a new approach to quantum simulation, with key advantages over arrays of conventional quantum dots. Because the metallic component of these hybrid islands has a quasi-continuous level spectrum, each site in an array can be effectively electronically identical; in contrast, each conventional semiconductor quantum dot has its own spectral fingerprint. Meanwhile, the semiconductor component retains gate-tunability of intersite coupling. This combination creates a scalable platform for simulating correlated ground states driven by Coulomb interactions. We report the fabrication and characterization of hybrid metal-semiconductor islands, featuring a submicron metallic component transparently contacting a gate-confined region of an InAs quantum well with tunable couplings to macroscopic leads. Tuning to the weak-coupling limit forms a single-electron transistor with highly-uniform Coulomb peaks, with no resolvable excitation spectrum in the Coulomb diamonds. Upon increasing the transmissions toward the ballistic regime we observe an evolution to dynamical Coulomb blockade.

## I. INTRODUCTION

Our best way to understand correlated electron behavior in exotic materials is to try to describe those materials through simplified effective Hamiltonians. Yet even these simplified Hamiltonians are often too computationally intensive to solve

in detail. This has spurred efforts to build tunable experimental realizations of such Hamiltonians, to measure their properties instead of calculating them on a conventional classical computer. One prominent approach to realizing such Hamiltonians is based on few-site semiconductor quantum dot arrays [1–4]. The strong Coulombic onsite energy  $U$ , electrostatic tunability of tunnel couplings  $\mathcal{T}_{\text{tunnel}}$ , and low carrier temperature  $T \ll U/k_B$ , where  $k_B$  is the Boltzmann constant, provide access to a parameter space favorable for studying strongly interacting ground states and quantum phase tran-

---

\* These authors contributed equally to this work.

sitions among them. Exotic phases and critical states simulated in this way include the Mott insulator [5], resonating valence bonds [6], Nagaoka ferromagnetism [7], and single and two-channel Kondo critical points [8–10]. To connect to bulk material properties, scaling up to larger arrays will be important. Challenges to such scaling include gate fanout [11], cryostat wiring and control interface limitations [12], and inter-dot crosstalk [13], forcing the design of shared gate architectures [14, 15] which require high dot-to-dot homogeneity [16]. Borsoi et al. [14] demonstrated shared gate control of a  $4 \times 4$  Ge crossbar array, tuning all 16 dots to single-electron occupancy. The 10-20% variation in the hole addition energies observed in the crossbar array represents a challenge for the homogeneity requirements of scalable quantum simulation. Although complementary metal-oxide-semiconductor (CMOS) compatible industrial fabrication processes have shown remarkable yields  $>96\%$  for Si quantum dots on 300-mm wafers, the voltage levels needed to tune to single-electron occupancy still show variations  $>5\%$  between matched pairs of dots [17]. While tuning large arrays is already challenged by variability in operating parameters, significant inhomogeneities persist even when each site is tuned to the single-electron limit. In particular, variations in excitation spectra, charging energies, and inter-dot tunnel couplings present a major obstacle to realizing large arrays with essentially identical sites, necessary for probing bulk material properties.

A new platform based on hybrid metal-semiconductor islands can solve part of this problem. The individual sites consist of gate-confined regions on a semiconducting two-dimensional electron gas (2DEG), with a metallic local density of states, and tunable coupling to reservoirs and neighboring sites through one-dimensional channels. This is realized by electrically connecting a submicron metal island to a comparably-sized region of 2DEG, bordered by quantum point contacts which act as tunable tunnel barriers. Fine tuning and convenient measurement of these barriers' transmission is made possible by operating at high magnetic field such that the 2DEG is in an integer quantum Hall state. A schematic of the device design is shown in Fig. 1. The energy spectrum of the confined region is characterized by a charging energy  $E_c = e^2/2C$ , where  $C$  is the total capacitance of the device, determined by the geometry of the island and gate electrodes. The metallic density of states in this region is insensitive to the confinement potential landscape, allowing each site to behave essentially identically, while the semiconductor component retains the ability to tune intersite coupling. Recent experiments on a pair of hybrid metal-GaAs quantum dots investigated a non-Fermi liquid quantum critical point (QCP) between competing 'charge'-Kondo ground states [18–20]. Scaling this to many such sites will allow the simulation of Kondo lattice models and the investigation of lattice coherence in heavy-fermion materials.

In a hybrid dot, melding a metallic density of states with the tunability granted by a semiconductor requires a highly transparent contact on the submicron scale between the metal island and 2DEG [20]. This has been a formidable challenge in previous implementations using GaAs as the semiconductor:

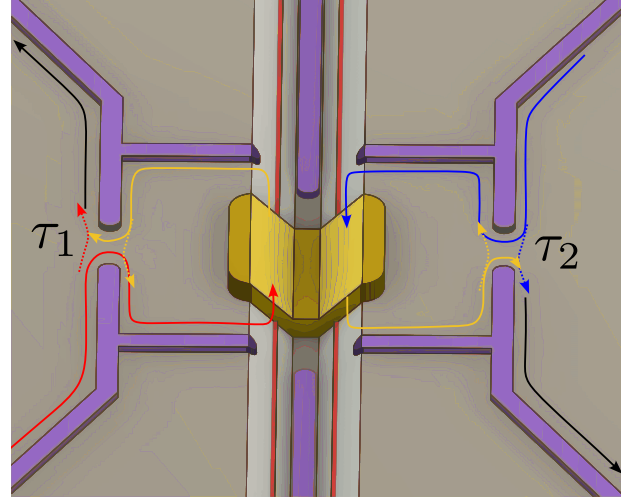


FIG. 1. **Device design schematic.** Schematic representation of the hybrid metal-semiconductor dot architecture. The InAs two-dimensional electron gas (gray) is confined with gate electrodes (purple) that realize a pair of quantum point contacts to tune the tunnel coupling to quantum Hall edge modes (red, blue) with transmissions  $\tau_{1,2}$ . A submicron metallic island strongly couples to and equilibrates the incident edge modes, resulting in a metallic density of states in the confined region and downstream (yellow) edge modes at the island electrochemical potential.

the midgap pinning of the Fermi level at the interface between the metal and the GaAs/AlGaAs heterostructures [21] requires the islands in Refs. [18–20] to be a few-microns-wide, limiting investigations of quantum critical phenomena to very low temperatures because of the small charging energy (300 mK) and leaving a narrow window between the latter and the lowest electron temperatures ( $\sim 20$  mK). The larger range of measurement temperatures enabled by a higher charging energy would allow for significantly more detailed quantitative analyses of low-temperature Kondo renormalization and quantum criticality [22].

InAs offers the prospect of higher charging energies due to more miniaturized ohmic contact to the semiconductor—Fermi level pinning above the conduction band minimum [21] obviates the need for annealed eutectic Au/Ge alloys, a major source of inhomogeneous contact morphology [23]. We report the fabrication and characterization of hybrid metal-InAs quantum dots, featuring a  $\sim 1 \mu\text{m}^2$  metallic island with tunable couplings to macroscopic reservoirs. In the quantum Hall regime, a near-perfect interface transparency ( $>99.2\%$ ) is measured for the outermost edge mode at quantum Hall filling factor  $\nu = 2$ . Quantum point contacts (QPCs) provide electric control of the dot-reservoir couplings. At weak tunneling we measure charge quantization with strong uniformity in Coulomb peaks, no resolvable excitation spectrum in the Coulomb diamonds (Fig 2.), and a four-fold enhancement in the charging energy over the GaAs platform. Using QPCs nominally identical to Ref. [24], we tuned the coupling strengths to reveal the evolution from static to dynamical Coulomb blockade, with charge quantization fully quenched when QPCs are opened to transmit a full mode. Our work

positions hybrid metal-InAs quantum dots as a candidate platform for making arrays of functionally identical sites to explore Kondo lattice coherence.

## II. DEVICE FABRICATION & MEASUREMENT SETUP

The devices featured in this work were fabricated on a heterostructure grown by molecular beam epitaxy on a semi-insulating InP (100) substrate. The layer structure is illustrated in Fig. S1(a) in the Supplemental Material (SM), with the growth parameters detailed in Ref [25] (Sample B). A 4 nm InAs quantum well sandwiched between 10.5 nm  $\text{In}_{0.75}\text{Ga}_{0.25}\text{As}$  layers forms the active region, and a 900 nm linearly graded  $\text{In}_x\text{Al}_{1-x}\text{As}$  strain-relaxed buffer layer reduces the dislocation density in the proximity of the quantum well. Finally, a 120 nm  $\text{In}_{0.75}\text{Al}_{0.25}\text{As}$  capping layer enhances mobility by moving the active region away from the top surface. The InAs quantum well is populated by unintentional impurities from deep-level donor states in the  $\text{In}_{0.75}\text{Al}_{0.25}\text{As}$  layers, with a density  $n = 4.5 \times 10^{11} \text{ cm}^{-2}$  and mobility  $6 \times 10^5 \text{ cm}^2/\text{Vs}$  as measured in a 60- $\mu\text{m}$ -wide Hall-bar at 40 mK (see SM).

The devices were processed with electron beam lithography and a citric/phosphoric acid-based wet etchant to define the mesas (see SM for details). Aiming for a pristine metal-InAs interface on the submicron-scale, the Ti/Au edge contact to the quantum well was made immediately after a short HCl dip, avoiding any oxygen plasma, or *in situ* Ar ion mill to protect the exposed sidewalls of the quantum well. A 35 nm  $\text{HfO}_2$  gate dielectric layer was grown by atomic layer deposition at 150°C, followed by Ti/Au gate electrodes deposited over multiple steps, the narrowest gate arms being 100 nm wide for fine control of the electrostatic potential landscape.

The measurements reported here were performed in a dry  $\text{He}^3\text{-He}^4$  dilution refrigerator with a mixing base temperature  $T_0 = 34 \text{ mK}$ , over multiple cooldowns. Unless otherwise specified, an out-of-plane magnetic field  $B_\perp = 5.5 \text{ T}$  places the 2DEG in the integer quantum Hall phase with filling factor  $\nu = 3$  and counter-clockwise chirality. The vanishing longitudinal resistance, quantized Hall resistance, and chirality of current flow simplify the analysis of transport data, permitting a quantitative treatment of the conductance as a function of arbitrary tunnel couplings at the point contacts. Furthermore, the Zeeman effect lifts spin degeneracy and the QPCs enable a tunable coupling of a single spin-polarized edge channel at each end of the island.

Transport was measured by sourcing an ac current excitation  $I_{ac} = 500 \text{ pA} - 10 \text{ nA}$  at frequencies less than 100 Hz with a 100 M $\Omega$  bias resistor. The current is drained at both ends of the island through grounded contacts that were tied directly to the cold finger of the dilution refrigerator. The robust and broad quantum Hall plateau converts the source current into an on-chip differential voltage excitation  $V_{ac} = I_{ac} \times h/\nu e^2$ , where  $h/e^2$  is the resistance quantum. The voltage drop is measured between voltage probes downstream of (A) the hybrid quantum dot and (B) the grounded current drain, using standard lock-in techniques. For a perfectly transparent

metal-semiconductor interface, a Landauer-Büttiker treatment reveals the series conductance  $G$  through the device as

$$G = \nu \frac{e^2}{h} \frac{V_T}{V_T + V_R}, \quad (1)$$

where  $V_{T,R}$  correspond to the transmitted and reflected voltage drops, measured as described above.

Data from three devices are reported in this work, with differences in the gate and metal island geometry aimed at focusing investigations on island transparency (Device A) and hybrid quantum dot Coulomb blockade (Devices B, C). To study transparency of the island to quantum Hall edge modes, Device A features a submicron Ti/Au island making contact to the InAs quantum well over a trench on a bow-tie mesa, with a pair of QPCs used to independently probe the transparency of each edge mode. The QPCs are placed far from the island (60  $\mu\text{m}$ ) to suppress charging effects (see Sec. III). Devices B and C, by contrast, feature submicron islands with QPCs closer to the island (400 nm) to form hybrid quantum dots. Device B was used to study charge quantization and charge noise in Secs. IV,V while Device C was used for dynamical Coulomb blockade investigations in Sec. VI.

## III. TRANSPARENCY OF THE SUBMICRON METALLIC ISLAND TO QUANTUM HALL EDGE MODES

The quality of the ohmic contact made by a metal island is characterized by the reflection probability of the quantum Hall edge modes at the interface with the quantum well. Device A for measuring transparency involves a bow tie-shaped mesa with a narrow trench across its width. The wet etch process results in  $\sim 45^\circ$  sidewalls with a nominal trench width of 120 nm at an etch depth of 400 nm. A Ti/Au island with a  $0.7 \times 1.5 \mu\text{m}^2$  footprint is deposited across the trench and bridges the trench, making sidewall contact to the exposed InAs quantum well, while macroscopic ohmic pads serve as the source and grounded-drain terminals, and voltage probes. This geometry ensures that any current between the two mesa regions must flow through the metal island. Figure 2(a) shows the device geometry, with the cross-section in Fig. 2(c) depicting the trench with the metal island making sidewall contact to the quantum well. A pair of QPCs 60  $\mu\text{m}$  on either side of the island are used to selectively populate edge modes, allowing a thorough study of transparency as a function of edge state index.

For a perfectly transparent interface, the edge modes transmitted through the QPCs will fully equilibrate at the island. Fitting the measured downstream voltages  $V_T$ ,  $V_R$  to a Landauer-Büttiker model provides an estimate of transparency.

When the QPCs each transmit only the outermost edge mode, the reflected voltage ( $V_R^{\tau_{1,2}=1}$ ) normalized to its value

with the QPCs pinched-off ( $V_R^{\tau_{1,2}=0}$ ) is given by

$$V_{R,1} := \frac{V_R^{\tau_{1,2}=1}}{V_R^{\tau_{1,2}=0}} = 1 - \frac{t_1}{2\nu}, \quad (2)$$

where  $1 - t_1$  is the reflection probability of the outer edge mode at the island-quantum well interface, and  $\tau_{1,2}$  are the transmissions of the outer edge modes through the QPCs, and  $V_{R,i}$  is the normalized reflected voltage for  $\tau_{1,2} = i$ . Description of the model and a derivation of this expression are included in the SM. Figure 2(b) depicts the normalized reflected voltage  $V_{R,i}$  as a function of the QPC gate voltages, clearly showing regions of quantized plateaus corresponding to positive integer  $i \in \mathbb{Z}^+ \leq \nu$  edge modes transmitted through each QPC. From the average  $\langle V_{R,1} \rangle$  over the QPC gate voltage space corresponding to a transmitted single edge mode, we extract an outer edge mode transparency of  $t_1 > 98\%$  at the low-field end of the  $\nu = 2, 3, 4$  plateaus. For  $\nu = 2$ , the transparency of the outer edge mode  $t_1 > 99.2\%$  over the range of the quantum Hall plateau accessible with a field  $< 9.5$  T. The transparency of subsequent inner modes is markedly diminished, likely due to the increased separation from the physical interface. Analysis and discussion of inner edge mode transparencies are included in the SM. Furthermore, we observe a decrease in transparency of the edge modes with field over a given quantum Hall plateau for all the filling factors considered ( $\nu \in \{6, 5, 4, 3\}$ ). This requires further investigation, but we speculate the field-dependent inter-edge mode equilibration (see SM), together with the reduced transparency of inner edge modes, as a plausible explanation for the lower apparent transparency of the outer edge mode.

#### IV. STATIC COULOMB BLOCKADE IN THE WEAK COUPLING LIMIT

The device to study charge quantization (Device B) in a hybrid metal-semiconductor dot consists of a transparent sub-micron Ti/Au island flanked by QPC gates ( $\sim 400$  nm away, see Fig. 3(a)). The hybrid quantum dot is formed by applying a negative voltage to the QPC gates to deplete the quantum well underneath and confine the InAs around the metal island, enabling operation in a regime where thermal fluctuations are suppressed  $k_B T \ll E_c = e^2/2C$ , where  $C$  is the capacitance of the device. We tune both QPCs to the weak tunneling limit and sweep the plunger gate  $V_{pR}$  to measure thermally-broadened Coulomb resonances. The electronic level spacing in the metallic island is  $\delta = \frac{1}{\rho_F \Omega}$ , where  $\rho_F$  is the electronic density of states per unit volume at the Fermi level and  $\Omega$  is the volume of the island. For gold with  $\rho_F \approx 10^{47} J^{-1} m^{-3}$  and  $\Omega \approx 0.15 \mu m^3$ , the electronic level spacing  $\delta \approx 400$  peV  $= k_B \times 5$  mK. Since the electron temperature is at least three orders of magnitude hotter than  $\delta$ , we can approximate the metallic island with a continuum electronic level spectrum. Consequently, single-electron tunneling through the hybrid dot is described by inelastic sequential tunneling through the QPCs with the conductance across a Coulomb resonance given by Kulik and Shekhter [26],

$$G^{\text{theory}} = \frac{G_\infty}{2} \frac{\alpha \delta V_{pR}/k_B T}{\sinh(\alpha \delta V_{pR}/k_B T)}, \quad (3)$$

where  $G_\infty = e^2 \rho_{\text{dot}} (\Gamma_1^{-1} + \Gamma_2^{-1})^{-1}$  is the classical series conductance through the QPCs with tunneling rates  $\Gamma_{1,2}$  respectively,  $\rho_{\text{dot}}$  is the density of states at the Fermi level in the dot,  $\delta V_{pR}$  is the plunger gate offset from charge degeneracy, and the plunger gate lever arm  $\alpha$  is defined by the ratio of the plunger gate capacitance and the total capacitance of the dot. In typical few-electron semiconductor quantum dots,  $\rho_{\text{dot}}$  strongly depends on the electrostatic environment defined by the surrounding gate potentials, making it very sensitive to disorder in the underlying heterostructure. Furthermore, the tunneling rates  $\Gamma_{1,2}$  are proportional to the electron wavefunction overlap between the dot and leads, which can vary significantly for the electronic states participating in transport [27, 28]. This results in a distribution of Coulomb peak spacing and heights [29, 30]. However, the metallic island in the hybrid dot screens local inhomogeneities in the electrostatic environment, instilling an energy-independent quasi-continuum density of states. This results in a uniform peak height set by the QPC transmissions, and peak spacing  $\Delta$  proportional to the charging energy  $\Delta = 2E_c/e\alpha$ . Casting the tunnel rates in terms of the measurable edge state transmissions through the QPCs,  $\rho_{\text{dot}} h \Gamma_{1,2} = \tau_{1,2}$ , the peak conductance is expressed as

$$\frac{G_\infty}{2} = \frac{1}{2} \frac{e^2}{h} (\tau_1^{-1} + \tau_2^{-1})^{-1}, \quad (4)$$

The uniformity in the Coulomb peak amplitudes over 17 successive Coulomb peaks is shown in Fig. 3(b). The peak amplitude  $G_{\text{peak}} = 0.186 \pm 0.001 e^2/h$ , computed by fitting every peak and reporting the mean weighted by the uncertainty of each fit. Equation 3 fits the peak for an electron temperature  $T = 54$  mK (Fig. 3(d)). The charging energy is estimated by adding a dc bias current to the ac excitation, and measuring the height of the corresponding Coulomb diamonds as shown in Fig. 3(c). We report a charging energy  $E_c \approx 100$   $\mu$ eV, about a four-fold enhancement over hybrid dots on a GaAs/AlGaAs platform [18, 31]. The plunger-gate tunability of the charge, the uniformity in  $E_c$  estimated from the diamond heights, and the lack of an excited electronic level spectrum are tell-tale signatures of a hybrid metal/semiconductor quantum dot. The metallic island in our device is much smaller (area  $\approx 1 \mu m^2$  compared with  $\approx 30 \mu m^2$  in Refs. [18, 31]), made possible by the high transparency ohmic contact afforded by the lack of a Schottky-barrier at metal/n-InAs interfaces [21]. However, the  $E_c$  boost is only modest due to the high- $\kappa$  ALD-grown  $HfO_2$  gate dielectric used in our devices. Furthermore, the 400 nm isotropic wet-etch process forces a 1  $\mu m$  lower bound on the island dimension across the trench (see Fig. 2(c)). The design of heterostructures requiring shallower etch depths, and process optimization for anisotropic etch profiles is currently under investigation and will be discussed in future work.

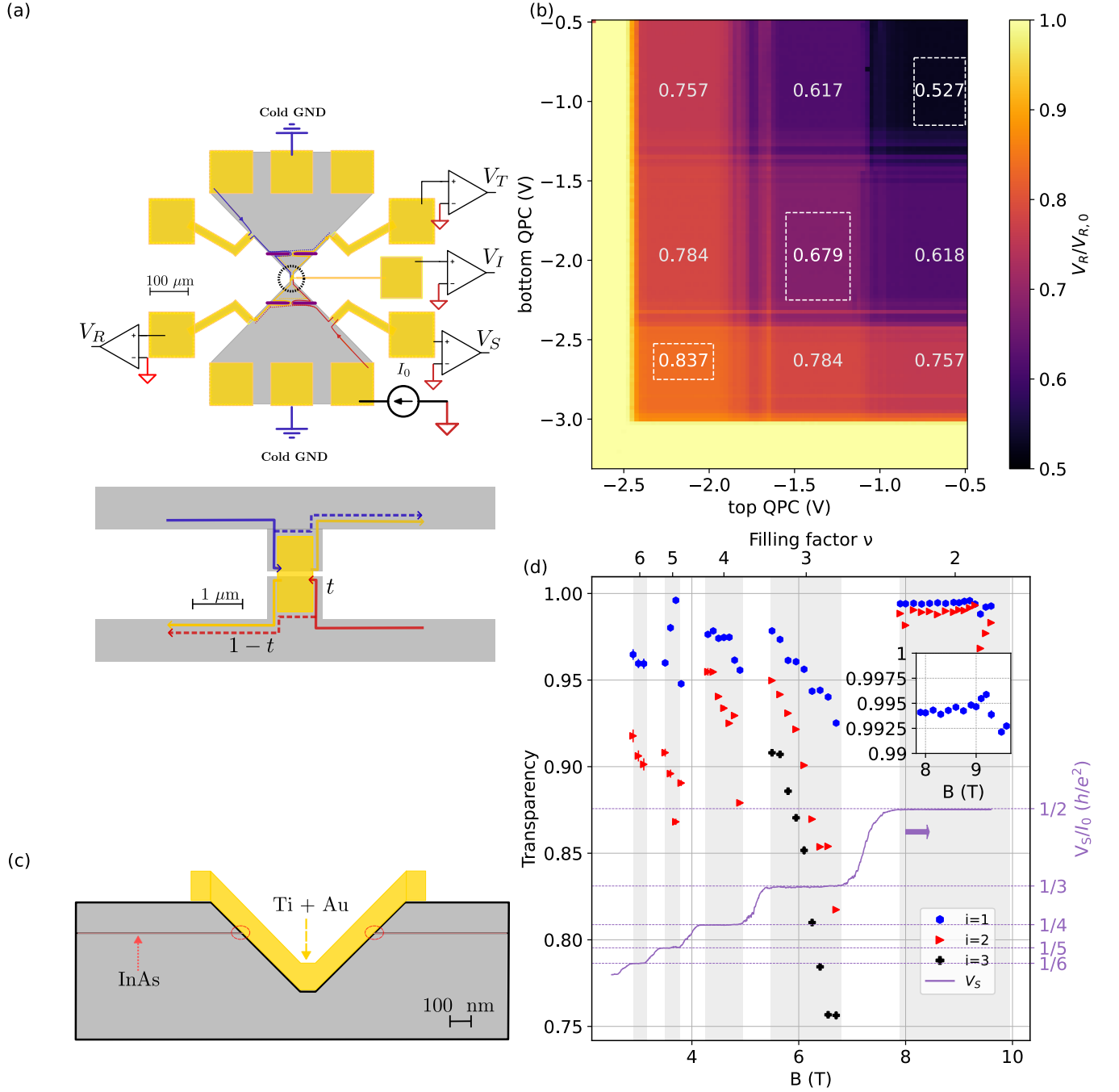


**FIG. 2. Edge state transparency.** (a) Schematic representation of Device A and the measurement setup. The  $0.7 \times 1.5 \mu\text{m}^2$  Ti/Au island is evaporated over a trench on a  $1.1\text{-}\mu\text{m}$ -wide mesa region (dashed outline) expanded in the bottom panel, of a “bow tie” mesa (gray) with macroscopic Ti/Au ohmic contacts and voltage probes (yellow). The QPC gates (purple) are symmetrically biased with dc voltage sources and are tuned to transmit an integer number of quantum Hall edge modes  $i$ . A pair of contacts on either end are tied to ground at the mixing chamber stage of the dilution fridge, and realize a “cold” ground to drain current. The device is biased with a 10 nA low-frequency ( $<20$  Hz) ac excitation. The voltage drop between the voltage probes and the cold ground are measured after amplification by lock-in amplifiers. The source ( $V_S$ ), reflected ( $V_R$ ), and transmitted ( $V_T$ ) voltages are measured  $\sim 160 \mu\text{m}$  from the island ( $V_I$ ). The red and blue edge modes are transmitted through the QPCs on the source and drain sides respectively, while the yellow modes emanate from the island. With a probability  $(1 - t_i)$ , the  $i$ -th outer edge mode is reflected at the interfaces as depicted in the bottom panel by dashed lines in the corresponding color. (b) Normalized reflected voltage as a function of the QPC gate voltages at  $B = 5.5$  T ( $\nu = 3$ ), clearly showing regions of quantized transport through each point contact, annotated with the average value for  $1 \leq p, q \leq 3$  transmitted edge modes through the top and bottom QPCs. The highlighted values for  $1 \leq i \leq 3$  is required for extracting the transparency for each edge mode, and are taken as the average value over the indicated region. (c) A cross-sectional view of the Ti/Au island making sidewall contact to the InAs quantum well, with the interface marked with red dashed circles. (d) Edge state transparency as a function of field for  $2 \leq \nu \leq 6$ , with the outermost edge mode indexed  $i = 1$ . The inset shows the outermost edge mode transmission  $t_1 > 99.2\%$  at  $\nu = 2$ .

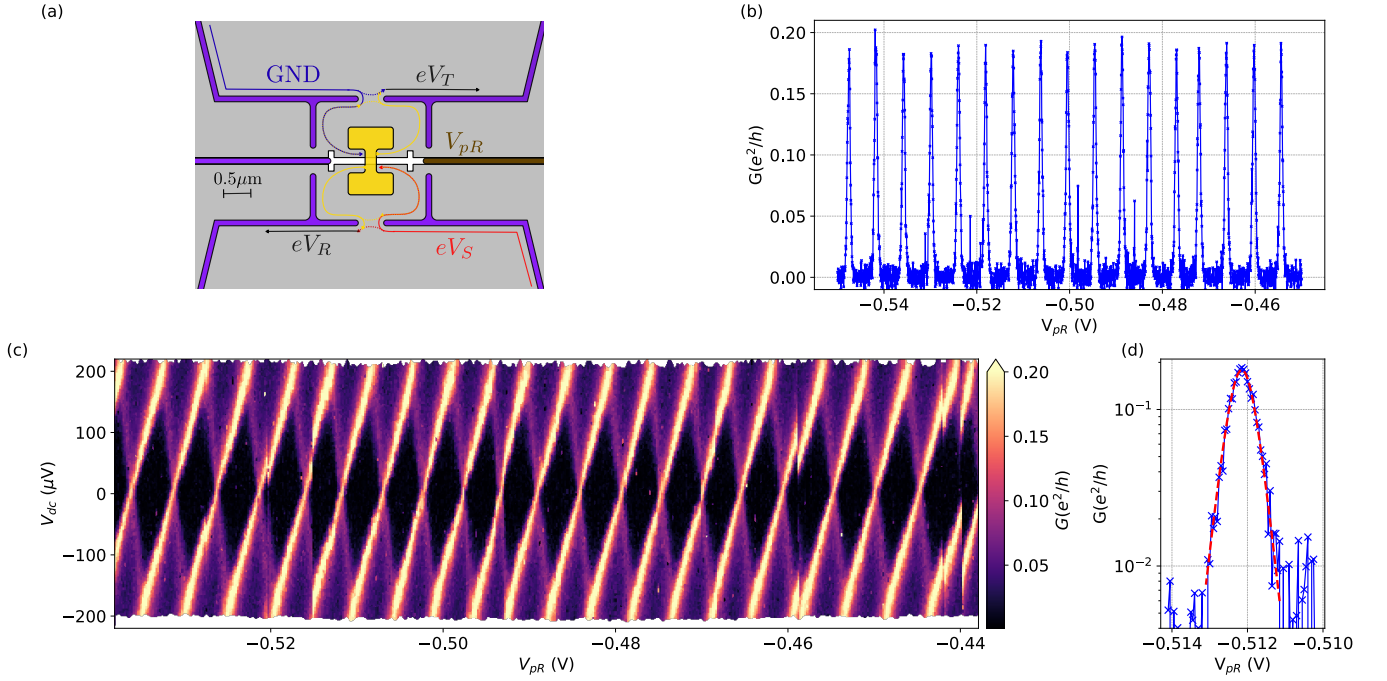


**FIG. 3. Static Coulomb blockade.** (a) Schematic of the hybrid metal-semiconductor quantum dot (Device B). An I-shaped Ti/Au island with a  $0.8 \times 1.2 \mu\text{m}^2$  footprint makes sidewall contact to the InAs quantum well across a 120 nm wide trench (white) on a mesa (gray). The QPC and plunger gates (purple, red) are biased with dc voltage sources, and the right plunger (red) is swept to reveal Coulomb blockade oscillations. The device is biased with a 500 pA low-frequency ( $< 30$  Hz) ac excitation and a dc current bias  $i_{dc}$ . A pair of contacts on either end are tied to ground at the mixing chamber stage of the dilution fridge, and realize a “cold” ground to drain current. The source ( $V_S$ ), reflected ( $V_R$ ), and transmitted ( $V_T$ ) voltage drops to ground are measured  $\sim 45\text{-}\mu\text{m}$  from the island after amplification by lock-in amplifiers. (b) Coulomb blockade oscillations in the series conductance  $G$  as a function of the plunger gate voltage  $V_{pR}$  for a set of 17 successive charging events, with the QPCs tuned to the weak tunneling limit  $\tau_{1,2} \ll 1$ . The high density of states at the metallic island results in uniform peak  $G = 0.186 \pm 0.001 e^2/h$ , with an amplitude and width determined by  $\tau_{1,2}$  and the ratio of the capacitive lever arm  $\alpha$  and temperature  $T$ , respectively. (c) Coulomb diamonds measured by a dc current  $|I_{dc}| < 25$  nA. The source dc voltage drop  $V_{dc} = I_{dc} \times h/3e^2$  is measured using a multimeter. The charging energy estimated from the diamond heights  $E_c = e^2/2C = 100 \mu\text{eV}$ , where  $C$  is the capacitance of the hybrid dot. (d) A Coulomb peak from (a) on a semi-log scale fit to Eq. 3 for determining the electron temperature  $= 54$  mK.

### A. Charge Noise

Charge quantization in the weak tunneling limit renders the hybrid dot sensitive to fluctuations in the effective chemical potential. This charge noise can result from metastable two-level fluctuators (TLFs) [32, 33] in the heterostructure stack and the gate dielectric, that may involve a combination of unintentional charged donor impurities, vacancy defects, and interface charge traps [34–37]. Abrupt switching characteristics reminiscent of telegraph noise from an ensemble of TLFs [38–40], and low-frequency drift in the gate voltages are the primary symptoms of charge noise in our devices. While the fluctuations in effective chemical potential introduces an artificial broadening of Coulomb peaks, it can also destabilize fragile quantum critical points that are sensitive to the chemical potential [41]. Charge noise spectroscopy is a valuable tool to understand dominant mechanisms, compare materials and processing techniques, and design measurement protocols for noise immunity [42–44].

Using a combination of techniques, we report the charge noise spectrum over 6 decades in frequency from 100  $\mu\text{Hz}$  to 100 Hz. At frequencies above 10 mHz, we use the Coulomb

peak flank (CPF) method, where the plunger gate voltage is parked on the steepest point of the Coulomb peak and a time-trace of the conductance is recorded. The measurement setup is illustrated in Fig. 4(a), with the parameters described in the SM. The conductance noise power spectral density (PSD) is then translated to charge noise using a linear approximation to the Coulomb peak

$$S_G = \left( \frac{\partial G}{\partial V_{pR}} \right)^2 \alpha^{-2} S_\mu, \quad (5)$$

where  $S_G$ ,  $S_\mu$  are the conductance noise and charge noise PSDs respectively, and  $\alpha$  is the lever arm extracted from the Coulomb diamond measurement in Fig. 3(c). This method assumes a small enough charge noise for the linear approximation to hold [27], which places an upper bound on the sampling time before low-frequency drift becomes dominant. Figure 4(b) shows a representative conductance peak  $G(V_{pR})$ , and the corresponding transconductance  $dG/dV_{pR}$ . The CPF time-trace is recorded with  $V_{pR}$  tuned to maximize  $dG/dV_{pR}$  (magenta circle) with a lock-in buffer for 1000 seconds, at a sampling rate of 300 samples per second. The



lock-in excitation frequency  $f_{lo} = 88$  Hz, and 3-dB bandwidth  $f_{3dB} = 80$  Hz were chosen to extract device charge noise from other sources in the measurement setup. The corresponding charge noise PSD averaged over 14 peaks is shown in Fig. 4(e). The measured charge noise resembles a  $1/f^\beta$  spectrum with  $\beta = 1.06$ , and  $S_\mu(1 \text{ Hz}) \sim 0.45 \pm 0.11 \text{ } \mu\text{eV}^2/\text{Hz}$ . The exponent  $\beta = 1$  is a signature of an ensemble of TLFs with switching rates in the measurement bandwidth, and a near-uniform distribution of activation energies [45, 46]. Unlike few-electron semiconductor dots [47], we do not observe a strong dependence of charge noise on the choice of Coulomb peak in the many-electron hybrid dot, see SM for individual peak PSDs.

At frequencies below 10 mHz, the slow drift renders the linear approximation invalid. Consequently, we resort to the Coulomb peak tracking (CPT) method, where a single Coulomb peak is repeatedly and synchronously swept back-and-forth, and the peak position in plunger gate voltage forms the time-series data [48]. We record data for 10,000 seconds with sweeps that last  $t_{\text{meas}} = 47$  seconds in each direction. Using the lever arm  $\alpha$ , the corresponding PSD is translated to charge noise, over a bandwidth spanning 100  $\mu\text{Hz}$  - 10 mHz. The noise PSD resembles a Lorentzian spectrum with exponent  $\beta = 1.86$ , implying strong coupling to a few TLFs with switching rates in the CPT measurement bandwidth [38–40].

We next discuss key features of the charge noise spectrum. First, our results indicate a power law  $1/f^\beta$ -like noise spectrum for the measured frequency ranges, with an exponent  $\beta$  that depends on the measurement protocol and bandwidth. This provides evidence for an inhomogeneous distribution of TLFs [49], with  $\beta = 1.86$  pointing to a few strongly coupled TLFs switching in the CPT measurement bandwidth (100  $\mu\text{Hz}$  - 10 mHz) [44, 46]. The distribution of TLFs with switching rates  $> 10$  mHz is more homogeneous, resulting in PSD that resembles a  $1/f^\beta$  spectrum with  $\beta = 1.06$ .

Second, we report a charge noise of  $0.45 \text{ } \mu\text{eV}^2/\text{Hz}$  at 1 Hz, averaged over 14 peaks. This compares favorably to the lowest reported value of  $1 \text{ } \mu\text{eV}^2/\text{Hz}$  at 1 Hz for quantum dots in III-V materials [50, 51], but is higher than or comparable to the  $0.11\text{--}0.88 \text{ } \mu\text{eV}^2/\text{Hz}$  range reported for single-electron quantum dots in undoped Si/SiGe heterostructures [49, 52]. This elevated noise, despite operating in the many-electron regime with a metal island, highlights the role of unintentional dopants in the heterostructure [25] and charge traps in the 35 nm ALD-grown  $\text{HfO}_2$  dielectric.

The RMS electrochemical potential noise associated with the measurement of a single Coulomb peak is given by [53]

$$\sigma_\mu = \sqrt{\int_{f_0}^{f_1} S_\mu(f) df} = 2.2 \text{ } \mu\text{eV}, \quad (6)$$

where the  $1/f^\beta$  spectral density results in a quasistatic regime dominated by low-frequency charge noise. The lower cutoff frequency is set by the inverse of the single-shot measurement time,  $f_0 = 1/t_m = 2.86 \text{ Hz}$ , for  $t_m = 350 \text{ ms}$ . The upper cutoff is estimated as  $f_1 = k_B T/h \approx 1 \text{ GHz}$ , corresponding to the energy scale beyond which charge quantization is thermally suppressed.

In this estimate of  $\sigma_\mu$ , we neglect contributions from fluctuations in the QPC transmissions  $\tau_{1,2}$  and from Johnson–Nyquist noise in the electron reservoir. The former is justified by the weak sensitivity of the measured conductance to variations in  $\tau_{1,2}$ , i.e.,  $|\partial G_{\text{peak}}/\partial V_{\text{qpc}}| \ll |\partial G/\partial V_{pR}|$ , where  $V_{\text{qpc}}$  is the QPC gate voltage and  $G_{\text{peak}}$  is the conductance at charge degeneracy ( $\delta V_{pR} = 0$ ), as demonstrated in the SM.

The contribution from Johnson–Nyquist noise is estimated for the 2DEG at  $T_e = 54 \text{ mK}$  and filling factor  $\nu = 3$ , yielding a white noise power spectral density [54, 55]

$$S_J = \frac{4\hbar\nu k_B T}{e^2} \approx 4 \times 10^{-9} \text{ } \mu\text{V}^2/\text{Hz}, \quad (7)$$

$$V_J = \sqrt{\int_{f_0}^{f_1} S_J(f) df} = 2 \text{ } \mu\text{V}, \quad (8)$$

which is small compared to the source-drain bias amplitude  $V_s = I_{\text{ac}} \times h/3e^2 = 43.02 \text{ } \mu\text{V}$  applied via ac current excitation. This supports the assumption that conductance noise primarily reflects fluctuations in the electrochemical potential  $\sigma_\mu$ , rather than thermal noise in the reservoir.

Fluctuations in the electrochemical potential can lead to broadening of the Coulomb peak lineshape. The estimate from Eq. 6 corresponds to a 1.5% increase in the full width at half maximum (FWHM) relative to the ideal thermal lineshape given in Eq. 3 for  $T_e = 54 \text{ mK}$  (see SM). This modest increase confirms that thermal fluctuations remain the dominant broadening mechanism, supporting the use of Coulomb peak width as a reliable proxy for electron temperature.

Finally, we consider the implications of  $\sigma_\mu$  for the stability of fragile quantum critical points in the context of quantum simulation. The ratio  $\sigma_\mu^2/E_c \approx 0.8 \text{ mK}$  defines a characteristic temperature scale  $T^*$ , below which charge noise is expected to destabilize the quantum critical point in the charge Kondo model [22]. Since this estimate of  $T^*$  is at least an order of magnitude smaller than the minimum electron temperature achieved in our device ( $T_e = 54 \text{ mK}$ ), we expect the quantum critical point to remain robust against charge noise in future investigations of lattice models based on charge Kondo interactions.

## V. CHARGE QUANTIZATION IN THE HYBRID DOT IN THE NEARLY BALLISTIC LIMIT

The weak tunnel coupling of the hybrid dot to its leads considered in the previous section suppresses charge fluctuations between the dot and the leads at low temperatures  $k_B T \ll E_c$ , resulting in a discrete many-body spectrum characterized by the charge of the hybrid dot [27]. Stronger coupling to the leads introduces fluctuations, relaxing charge quantization in the hybrid dot [56–61]. Smooth electrostatic control of edge mode transmissions  $\tau_{1,2}$  through the QPCs enables a systematic study of the evolution of charge quantization from the weak to strong tunneling limit, before quantum fluctuations entirely quench charge quantization in the ballistic ( $\tau = 1$ ) limit of either QPC [31]. This is in contrast to mesoscopic

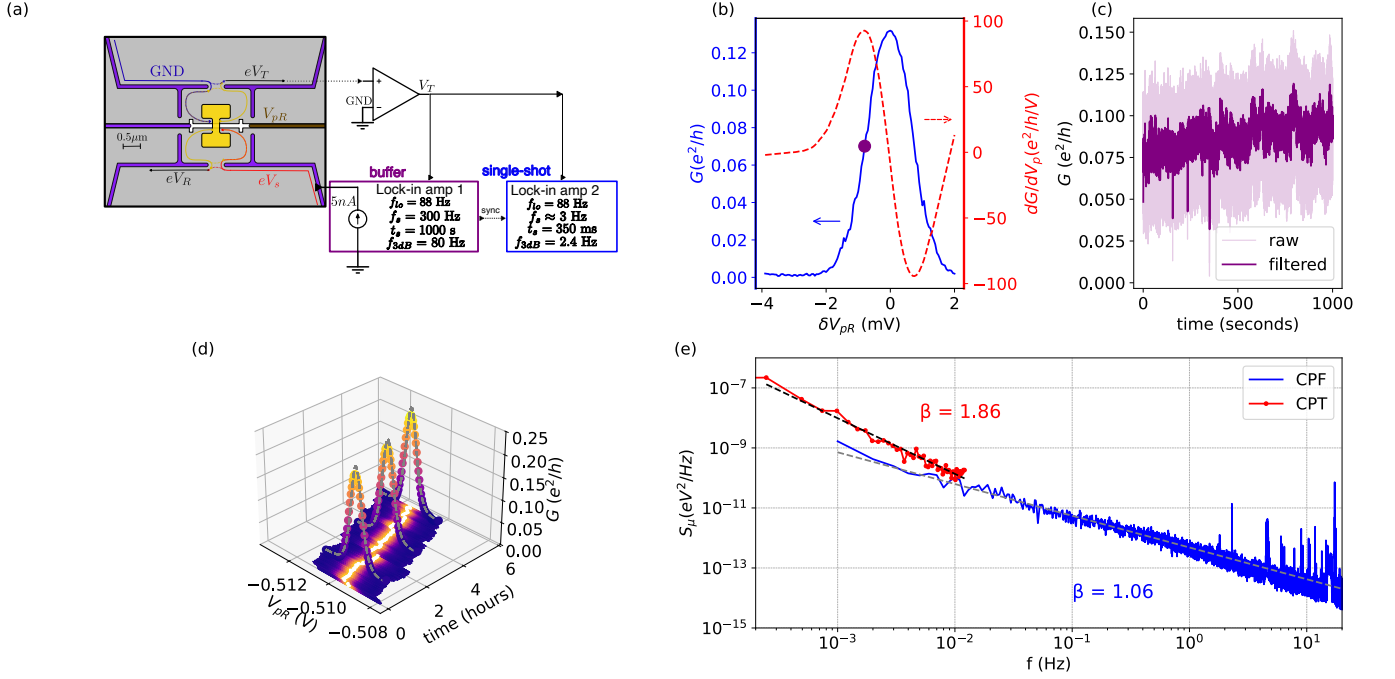


FIG. 4. **Charge noise.** (a) Schematic representation of the measurement setup. The device is biased with a  $5 \text{ nA} \times 25813/\nu \approx 43 \text{ } \mu\text{V}$  for  $\nu = 3$ . After pre-amplification, the time-series data of the voltage drop  $V_T$  between the corresponding voltage probe and on-chip cold-ground is recorded in a lock-in amplifier internal buffer, for 1000 seconds, sampled at 300 Hz, with a time-constant of 3 ms. Low-bandwidth single shot measurements are recorded with a synced lock-in for resolving the Coulomb peak and identifying the flank – the plunger gate tuning corresponding to the maximum transconductance  $dG/dV_{PR}$ . (b) Representative Coulomb peak (blue) and transconductance (red) as a function of plunger gate voltage  $V_{PR}$ . In the Coulomb peak flank method, the plunger gate is parked on the flank of the Coulomb peak (magenta circle), where the transconductance is maximized. (c) Time series data of  $G$  at the flank of the Coulomb peak. (d) Coulomb peak tracking measurements highlighting 3 Coulomb peaks with the fits to Eq. 3. The white points on the heatmap indicate the peak positions used to calculate the low frequency PSD. (e) PSD of the charge noise extracted from the Coulomb peak flank (blue) and Coulomb peak tracking methods with bidirectional (red) fit to a  $f^\beta$  power-law. The best-fit  $\beta = 1.06$  (1.86) for CPF (CPT) resembles a  $1/f$  ( $1/f^2$ ) spectrum.

Coulomb blockade observed in semiconductor dots, where the interplay of coherence and Coulomb interactions drives charge quantization, evinced by Coulomb oscillations even in the limit of a fully transmitting mode through each QPC [57]. The continuum single-particle electronic level spectrum of the hybrid dot suppresses elastic cotunneling across the Coulomb barrier, enabling independent treatment of the point contacts. Transport in the hybrid dot is a realization of the inelastic cotunneling model studied by Furusaki and Matveev [62], and is distinct from Yi and Kane’s analysis [63] of charge quantization in a phase coherent quantum dot coupled to leads in the quantum Hall regime.

As was demonstrated on a GaAs/AlGaAs heterostructure [31], a hybrid dot architecture with (i) charge quantization robust to thermal fluctuations  $k_B T \ll E_c$ , (ii) plunger-gate tunable charge, and (iii)  $\tau_{1,2}$  that can be tuned and measured independently, is an ideal testbed for Coulomb blockade theory with arbitrary couplings to the leads, beyond the limits accessible by analytical methods based on perturbation and bosonic field theories [26, 27, 62]. Although this device realizes the first two requirements by design, dynamical Coulomb blockade (DCB) renormalization challenges an independent measurement of intrinsic transmissions  $\tau_{1,2}$  [64].

Section VI describes the DCB-suppression of intrinsic transmission  $\tau_{1,2} \rightarrow \tilde{\tau}_{1,2}$ , and the measurement protocol to extract  $\tau_{1,2}$  from measurements of renormalized  $\tilde{\tau}_{1,2}$ .

The degree of charge quantization is characterized by the visibility of conductance oscillations  $Q$  as a function of  $V_{PR}$ , and is defined as

$$Q = \frac{\max G(V_{PR}) - \min G(V_{PR})}{\max G(V_{PR}) + \min G(V_{PR})}, \quad (9)$$

where  $\max$  ( $\min$ ) return the maximum (minimum) conductance over one  $V_{PR}$  period  $\Delta$ . The visibility of conductance oscillations  $Q$  is directly proportional, with an order unity coefficient, to the visibility of charge oscillations accessible in capacitance measurements, thus providing a quantitative estimate of charge quantization in a transport measurement [31, 63].

We study the evolution of  $Q$  with transmission of the outer edge mode at each QPC by measuring  $G(V_{PR})$  in Fig. 5(c)-(f) for a fixed  $\tau_1 = 0.747 \pm 0.015$ , while tuning  $\tau_2$  between each panel, with the uncertainties reported as the standard deviation over a plunger gate sweep over a  $3\Delta$  range. In the ballistic limit ( $\tau_2 = 1$ ) the charge fluctuations are on the order of



the electron charge. Charge quantization is quenched ( $Q = 0$ ), and the measured  $G$  is independent of  $V_{pR}$  (see Fig. 5(c)). As the top QPC is tuned away from the ballistic limit ( $\tau_2 < 1$ ), fluctuations are suppressed and  $G(V_{pR})$  oscillates with the period  $\Delta$  characteristic of Coulomb blockade. The presence of Coulomb peaks with near-zero conductance in the valleys for  $\tau_2 \leq 0.90$  is a signature of the robustness of charge quantization over a wide range of transmissions, corroborating observations by Jezouin, et al. [31] in a GaAs/AlGaAs heterostructure.

Figure 5(a) shows the evolution of charge quantization as  $\tau_2$  is smoothly tuned away from the ballistic limit ( $\tau_2 = 1$ ) to  $\tau_2 \gtrsim 0.5$  as the bottom QPC is stepped through  $\tau_1 \in [0.258, 0.999]$ . In the weak backscattering limit ( $1 - \tau_2 \ll 1$ ),  $Q$  is a strong function of  $\tau_2$ , and increases rapidly as the coupling to the outer edge mode is reduced. As  $\tau_2$  is further reduced, ( $\tau_2 < 0.7$ ),  $Q$  stays nearly constant, providing further evidence for the robustness of charge quantization to fluctuations.

In the presence of a nearly-ballistic channel ( $1 - \tau_2 \ll 1$ ), a bosonization approach predicts a  $\sqrt{1 - \tau_2}$  scaling of charge quantization for  $k_B T \ll E_c$ , irrespective of the transmission of the second channel [65]. Specifically, when both the channels are coupled in the near-ballistic limit,

$$Q(\sqrt{1 - \tau_{1,2}} \ll 1) = \frac{\gamma}{\pi} \frac{E_c}{k_B T} \sqrt{(1 - \tau_1)(1 - \tau_2)}, \quad (10)$$

where  $\gamma = \exp(C)$ , with  $C \approx 0.5772 \dots$  being the Euler's constant. The scaling near the ballistic limit of  $\tau_2$  is depicted by plotting  $Q$  as a function of  $1 - \tau_2$  in Fig. 5(b). The asymptotes for  $\sqrt{1 - \tau_{1,2}} \ll 1$  given by Eq. 10 are shown as dashed lines and reveal the  $\sqrt{1 - \tau_2}$  scaling, with the prefactor left as a fit parameter. The nonasymptotic predictions based on strong inelastic cotunneling [62] (see SM) are shown as solid curves for  $(1 - \tau_{1,2}) < 0.01$ , with  $\tau_1$  left as a fit parameter to account for drift over the course of  $G(V_{pR})$  measurements for a fixed voltage on the bottom QPC. While the  $\sqrt{1 - \tau_2}$  scaling behavior is in qualitative agreement, the deviations with the nonasymptotic predictions are likely due to a renormalization due to dynamical Coulomb blockade, as discussed in the next section. A device architecture permitting an independent measurement of  $\tau_{1,2}$  would provide further quantitative insights into charge quantization in the presence of quantum fluctuations, and enable investigations of critical scaling in the proximity of phase transitions, as in the multi-channel charge Kondo model [19, 20, 62].

## VI. DYNAMICAL COULOMB BLOCKADE IN THE BALLISTIC LIMIT

Although charge quantization is quenched in the ballistic limit  $\tau_2 = 1$ , features of Coulomb interactions persist, evidenced in the low-bias suppression of  $G$  for  $\tau_1 < 1$  through dynamical Coulomb blockade (DCB). This suppression results from the granularity of electronic charge tunneling through the top QPC, and the finite time constant of the relaxation of electromagnetic modes excited in the resistive environment

each time an electron tunnels through the point contact. Considering the bottom QPC, its environment can be modeled as a transmission line with a resistance controlled by transmission through the top QPC ( $R_{\text{env}} = (1/\tau_2)h/e^2$ ), and a capacitance set by the hybrid dot  $E_c = e^2/2C$ . The tunneling of a single electron through the constriction defined by the bottom QPC displaces the electromagnetic modes in the environment out of equilibrium [66]. When  $R_{\text{env}} \sim h/e^2$ , the time constant for the relaxation of this charge excitation  $t_{\text{env}} = R_{\text{env}}C$ , is comparable to the time scale of Coulomb interactions,  $t_Q \sim h/E_c$ , resulting in charge fluctuations on the order of  $e$ . For a bias voltage  $V < E_c/e$ , the duration of the electron wavepacket  $t_e \sim h/eV$  exceeds the time scale over which Coulomb interactions set in  $t_e > t_Q \sim t_{\text{env}}$ . These Coulomb interactions in the dynamic regime result in the low bias suppression of tunneling conductance through the point contact. For a short conductor in the weak-tunneling limit ( $\tau \ll 1$ ), in the presence of environmental backaction, the suppression in zero-bias transmission was calculated by Joyez and Esteve [67] and reviewed in Ref. [68]. Kindermann and Nazarov [69] extended this to arbitrary mesoscopic conductors embedded in a purely dissipative environment, which was generalized to arbitrary environment resistances by Parmentier, et al. [64],

$$\frac{\tau(V)}{1 - \tau(V)} = \frac{\tilde{\tau}}{1 - \tilde{\tau}} \frac{E_B(R_{\text{env}}, V, T) + 1}{E_B(R_{\text{env}}, V = 0, T) + 1}, \quad (11)$$

where  $\tau(V)$  is the transmission at a bias voltage  $V$ ,  $\tilde{\tau}$  is the measured transmission at zero dc bias  $\tau(V = 0)$ ,  $E_B(R_{\text{env}}, V = 0, T) := \lim_{\tau \rightarrow 0} (\tilde{\tau} - \tau)/\tau$  is the relative circuit backaction for a tunnel junction in the same circuit. The backaction for arbitrary bias voltages  $E_B(R, V, T)$  can be computed using the dynamical Coulomb blockade framework for tunnel junctions (see SM).

A larger hybrid dot device (Device C) with  $E_c = 70 \mu\text{eV}$ , measured in a different cooldown with  $T = 60 \text{ mK}$  was tuned for characterizing DCB as depicted in Fig. 6(a) (see SM for the corresponding Coulomb diamond and electron thermometry data). The top QPC is set to transmit one (two) edge modes, resulting in an environment resistance  $R_{\text{env}} = h/e^2$  ( $h/2e^2$ ). Figure 6(b) shows the dc bias dependence of transmission through the bottom QPC  $\tau_1(V_{dc})$ , where each trace corresponds to a particular QPC gate voltage, as the QPC is opened from pinch-off. The transmission measured for a bias  $eV_{dc} \gtrsim E_c$  quenches the circuit backaction, revealing the intrinsic transmission  $\tilde{\tau}_1(V_{dc} \gtrsim E_c) \rightarrow \tau$ . The measured low bias ( $V_{dc} \ll E_c$ ) suppression of transmission is in agreement with predictions of Eq. 11 based on electron temperature  $T$ , charging energy  $E_c$ , environment impedance  $R_{\text{env}} = h/e^2$  and zero bias transmission  $\tilde{\tau}$ . However, there is a significant difference at high bias  $V_{dc} \geq E_c$ . This is likely due to the bias dependence of the intrinsic transmission through the saddle-point potential realized by the QPC [24], and the sample heating due to the d.c. current through the island at high transmissions [64], obscuring a direct measurement of the intrinsic  $\tau_1$ . Figure 6(d) highlights the suppressed transmission  $\tilde{\tau}_1$  as a function of QPC gate voltage extracted from a series conductance measurement  $\tilde{\tau}_1 = h/e^2 (G^{-1} - R_{\text{env}})^{-1}$  at zero dc

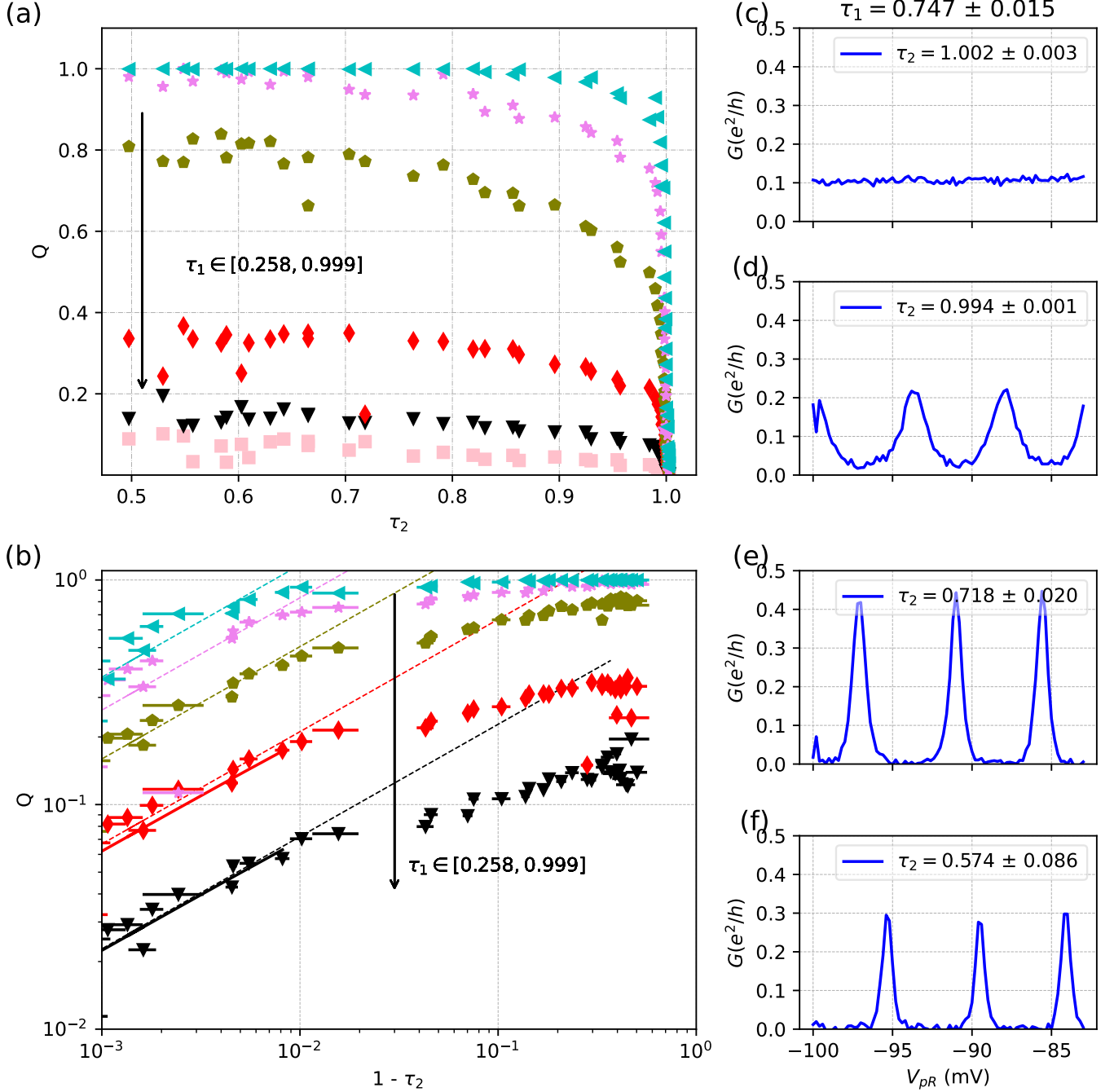


**FIG. 5. Controlling charge quantization** (a) The visibility of conductance oscillations  $Q$  as a function of the outer edge mode transmission through the top QPC  $\tau_2$ , for the transmission through the bottom QPC  $\tau_1 \in [0.258, 0.999]$ . (b) The recovery of  $Q$  as  $\tau_2$  is tuned away from the ballistic limit ( $1 - \tau_2 \ll 1$ ). The asymptotic  $\sqrt{1 - \tau_2}$  scaling given by Eq. 10 is shown as dashed lines with the prefactor left as a fit parameter. The solid curves for  $1 - \tau_{1,2} < 0.01$  (black, red) correspond to predictions based on strong inelastic cotunneling, with  $\tau_1$  left as a fit parameter. See text and SM for details. (c-f) Series conductance through the hybrid dot for a fixed  $\tau_1 = 0.747 \pm 0.015$ , as  $\tau_2$  is varied  $\in \{1.002, 0.999, 0.664, 0.574\}$  between the panels with uncertainties as indicated.

bias and  $V_{dc} = 116.2 \mu\text{V}$ , with the predicted  $\tau$  based on fits to Eq. 11 at every QPC gate voltage (Fig. 6(b)).

Equation 11 also predicts a circuit backaction  $\delta\tau/\tau := (\tilde{\tau} - \tau)/\tau$  proportional to  $(1 - \tilde{\tau})$  with a slope that depends on the ratio  $E_c/k_B T$  and  $R_{\text{env}}$ . This is depicted in Fig. 6(c)

for the bottom QPC, with the top QPC set to transmit one ( $R_{\text{env}} = h/e^2$ ) and two ( $R_{\text{env}} = h/2e^2$ ) edge modes. The magnitude of circuit backaction increases as the QPC is pinched-off, with  $\lesssim 90\%$  reduction in the intrinsic transmission measured for  $R_{\text{env}} = h/e^2$ . The solid lines represent the predicted

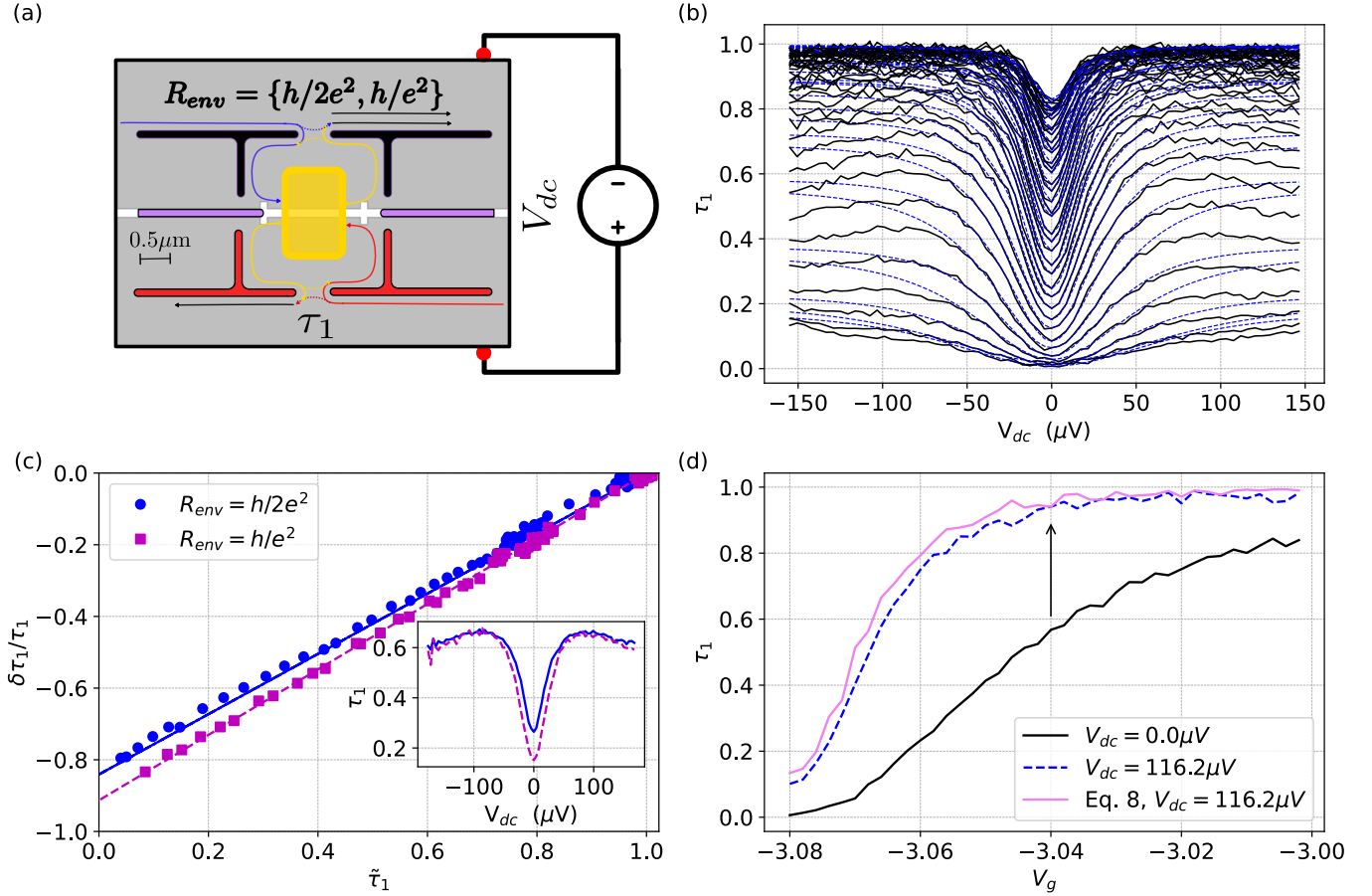


**FIG. 6. Dynamical Coulomb Blockade.** (a) Schematic representation of Device C and the measurement setup. The top QPC is set to transmit one (two) edge modes setting the environment resistance  $R_{env} = h/e^2$  ( $R_{env} = h/2e^2$ ). A dc current is added to the 500 pA ac current excitation to study the effect of circuit backaction. (b) The bottom QPC gate voltage is stepped up from pinch-off with the DC bias swept in the range  $|eV_{dc}| < E_c$ . The low bias  $|eV_{dc}| \ll E_c$  suppression of the transmission extracted from a series conductance measurement  $\tau_1 = h/e^2 (G^{-1} - h/e^2)^{-1}$ , is in agreement with the DCB predictions (Eq. 11), shown as blue dashed lines for every QPC gate voltage. (c) The relative circuit backaction as a function of the DCB-suppressed zero-bias transmission, with theoretical prediction for  $E_c = 70 \mu\text{eV}$ ,  $T = 60 \text{ mK}$ , and no fit parameters. The inset shows d.c. bias sweeps for the QPC with  $R_{env} = h/e^2, h/2e^2$  at different gate voltages for a  $\tau_1(100 \mu\text{V}) \approx 0.65$ , highlighting the increased backaction for the more resistive environment. (d) Bottom QPC transmission plotted as a function of QPC gate voltage at zero d.c. bias (solid black), and  $eV_{dc} = 116.2 \mu\text{V}$  (dashed blue), with the prediction from Eq. 11 in pink. The discrepancy between the measured high bias transmission and the predicted intrinsic  $\tau_1$  is likely due to the energy-dependence of the tunneling through the QPC, and the heating effect of the applied d.c. bias.

circuit backaction based on  $E_c$ ,  $T$ ,  $Z_{env}$ , and Eq. 11 with no fit parameters. Data and quantitative predictions are indistinguishable across the range of measured transmissions. The inset highlights the enhanced backaction for a more resistive environment by showing traces with  $\tau_1 \approx 0.65$ , but a markedly lower  $\tilde{\tau}_1 \approx 0.15$  for  $R_{env} = h/e^2$ , compared with  $\tilde{\tau}_1 \approx 0.28$  for  $R_{env} = h/2e^2$ .

The tunability of  $R_{env}$  and  $\tilde{\tau}_{1,2}$  enables a systematic study of circuit backaction through the QPC. The lack of a high bias plateau in the measured transmission presents a substantial challenge in calibrating  $\tau_{1,2}(V_g)$  in the current device architecture. Future generations will feature a gate-tunable switch to short-circuit the island and quench circuit backaction at zero dc bias [64].

## VII. CONCLUSION

We have presented the fabrication and characterization of hybrid metal-semiconductor devices in an InAs-based deep quantum well which displays near-perfect transparency of the outermost quantum Hall edge mode to a submicron Ti/Au metallic island. A set of gate electrodes confine the InAs quantum well around the metal-semiconductor interface to form a hybrid quantum dot, with QPCs providing tunability of the tunnel coupling to macroscopic reservoirs. In the weak tunneling limit, the hybrid displays single-electron transport with remarkable uniformity of Coulomb peak heights. The Coulomb diamonds reveal a  $100 \mu\text{eV}$  charging energy, providing access to the ratio of energy scales  $E_c/k_B T \leq 23$  with a base electron temperature  $T \sim 50 \text{ mK}$ , and is an important fig-

ure of merit quantifying the robustness of charge quantization to thermal fluctuations, necessary for enabling scaling studies in the vicinity quantum critical points [22]. This is similar to the  $E_c/k_B T \approx 26$  ratios accessible in previous works with a few micron-sized metallic island on a GaAs/AlGaAs platform [18, 20], however, without the demanding cryogenic requirements for the  $T = 12$  mK electron temperatures reported in those measurements. Further efforts to scale down the size of the hybrid islands to boost the charging energy are underway, and involve working with shallower etches, testing an anisotropic etch process, and moving the QPC gates closer to the island. Charge noise spectroscopy quantifies the effect of TLFs coupled to the dot, revealing a  $S_\mu = 0.45 \mu\text{V}^2/\text{Hz}$  noise at 1 Hz.

The smooth tunability of outer edge mode transmissions through the QPCs enables a systematic study of charge quantization, demonstrating a robustness to charge fluctuations with well-defined conductance peaks and valleys for  $\tau_{1,2} \leq 0.7$ . At the ballistic limit of either QPC, charge quantization is quenched although effects of Coulomb interactions persist in the form of dynamical Coulomb blockade, resulting in the low-bias  $|eV_{dc}| \ll E_c$  suppression of transmission. This study supports the prospect of using hybrid metal-InAs quantum

dots for emulating the physics of the multi-channel and multi-island Kondo model based on the charge pseudospin of the hybrid island [62]. This is a critical building block toward investigations of the Kondo lattice model [70] for gaining insights into lattice coherence observed in heavy fermion materials [71]. The data that support the findings of this study are available from the corresponding author upon request.

## VIII. ACKNOWLEDGMENTS

The authors thank B. Suo, W. Pouse, M. Pendharkar, C. Marcus, A. Mitchell, C. Mora, F. Pierre, and A. Anthore for their scientific insights and suggestions. Measurement and analysis were supported by the U.S. Department of Energy (DOE), Office of Science, Basic Energy Sciences (BES), under Contract No. DE-AC02-76SF00515, and the Gordon & Betty Moore Foundation under Grant No. GBMF9460. C.L.H. acknowledges support from the National Science Foundation (NSF) and Stanford Graduate Fellowship (SGF). Part of this work was performed at the Stanford Nano Shared Facilities (SNSF), supported by the National Science Foundation under Award No. ECCS-2026822.

- 
- [1] C. J. V. Diepen, T. K. Hsiao, U. Mukhopadhyay, C. Reichl, W. Wegscheider, and L. M. Vandersypen, Quantum simulation of antiferromagnetic heisenberg chain with gate-defined quantum dots, *Physical Review X* **11**, 10.1103/PhysRevX.11.041025 (2021).
  - [2] T. K. Hsiao, P. C. Fariña, S. D. Oosterhout, D. Jirovec, X. Zhang, C. J. V. Diepen, W. I. Lawrie, C. A. Wang, A. Sammak, G. Scappucci, M. Veldhorst, E. Demler, and L. M. Vandersypen, Exciton transport in a germanium quantum dot ladder, *Physical Review X* **14**, 10.1103/PhysRevX.14.011048 (2024).
  - [3] C. W. Kim, J. M. Nichol, A. N. Jordan, and I. Franco, Analog quantum simulation of the dynamics of open quantum systems with quantum dots and microelectronic circuits, *PRX Quantum* **3**, 10.1103/PRXQuantum.3.040308 (2022).
  - [4] J. Knörzer, C. J. V. Diepen, T. K. Hsiao, G. Giedke, U. Mukhopadhyay, C. Reichl, W. Wegscheider, J. I. Cirac, and L. M. Vandersypen, Long-range electron-electron interactions in quantum dot systems and applications in quantum chemistry, *Physical Review Research* **4**, 10.1103/PhysRevResearch.4.033043 (2022).
  - [5] L. M. Vandersypen, H. Bluhm, J. S. Clarke, A. S. Dzurak, R. Ishihara, A. Morello, D. J. Reilly, L. R. Schreiber, and M. Veldhorst, Interfacing spin qubits in quantum dots and donors—hot, dense, and coherent, *npj Quantum Information* **3**, 10.1038/S41534-017-0038-Y (2017).
  - [6] C. A. Wang, C. Déprez, H. Tidjani, W. I. Lawrie, N. W. Hendrickx, A. Sammak, G. Scappucci, and M. Veldhorst, Probing resonating valence bonds on a programmable germanium quantum simulator, *npj Quantum Information* **9**, 10.1038/s41534-023-00727-3 (2023).
  - [7] J. P. Dehollain, U. Mukhopadhyay, V. P. Michal, Y. Wang, B. Wunsch, C. Reichl, W. Wegscheider, M. S. Rudner, E. Demler, and L. M. Vandersypen, Nagaoka ferromagnetism observed in a quantum dot plaquette, *Nature* **579**, 528 (2020).
  - [8] D. Goldhaber-Gordon, H. Shtrikman, D. Mahalu, D. Abusch-Magder, U. Meirav, and M. A. Kastner, Kondo effect in a single-electron transistor, *Nature* **391**, 156 (1998).
  - [9] W. G. van der Wiel, S. D. Franceschi, T. Fujisawa, J. M. Elzerman, S. Tarucha, and L. P. Kouwenhoven, *At. Data Nucl. Data Tables*, Tech. Rep. (1985).
  - [10] R. M. Potok, I. G. Rau, H. Shtrikman, Y. Oreg, and D. Goldhaber-Gordon, Observation of the two-channel kondo effect, *Nature* **446**, 167 (2007).
  - [11] T. Nguyen, C. D. Hill, L. C. Hollenberg, and M. R. James, Fan-out estimation in spin-based quantum computer scale-up, *Scientific Reports* **7**, 10.1038/s41598-017-13308-0 (2017).
  - [12] D. J. Reilly, *Challenges in Scaling-up the Control Interface of a Quantum Computer*, Tech. Rep.
  - [13] B. Undseth, X. Xue, M. Mehmandoost, M. Rimbach-Russ, P. T. Eendebak, N. Samkharadze, A. Sammak, V. V. Dobrovitski, G. Scappucci, and L. M. Vandersypen, Nonlinear response and crosstalk of electrically driven silicon spin qubits, *Physical Review Applied* **19**, 10.1103/PhysRevApplied.19.044078 (2023).
  - [14] F. Borsoi, N. W. Hendrickx, V. John, S. Motz, F. V. Riggelen, A. Sammak, S. L. D. Snoo, G. Scappucci, and M. Veldhorst, *Shared control of a 16 semiconductor quantum dot crossbar array*, Tech. Rep.
  - [15] M. Künne, A. Willmes, M. Oberländer, C. Gorjaew, J. D. Teske, H. Bhardwaj, M. Beer, E. Kammerloher, R. Otten, I. Seidler, R. Xue, L. R. Schreiber, and H. Bluhm, The spinbus architecture for scaling spin qubits with electron shuttling, *Nature Communications* **15**, 10.1038/s41467-024-49182-4 (2024).
  - [16] R. Li, L. Petit, D. P. Franke, J. P. Dehollain, J. Helsen, M. Steudtner, N. K. Thomas, Z. R. Yoscovits, K. J. Singh, S. Wehner, L. M. K. Vandersypen, J. S. Clarke, and M. Veldhorst, *A crossbar network for silicon quantum dot qubits*, Tech. Rep. (2018).

- [17] S. Neyens, O. K. Zietz, T. F. Watson, F. Luthi, A. Nethewewala, H. C. George, E. Henry, M. Islam, A. J. Wagner, F. Borjans, E. J. Connors, J. Corrigan, M. J. Curry, D. Keith, R. Kotlyar, L. F. Lampert, M. T. Mądzik, K. Millard, F. A. Mohiyaddin, S. Pellerano, R. Pillarisetty, M. Ramsey, R. Savvitskyy, S. Schaal, G. Zheng, J. Ziegler, N. C. Bishop, S. Bojarski, J. Roberts, and J. S. Clarke, Probing single electrons across 300-mm spin qubit wafers, *Nature* **629**, 80 (2024).
- [18] W. Pouse, L. Peeters, C. L. Hsueh, U. Gennser, A. Cavanna, M. A. Kastner, A. K. Mitchell, and D. Goldhaber-Gordon, Quantum simulation of an exotic quantum critical point in a two-site charge kondo circuit, *Nature Physics* **19**, 492 (2023).
- [19] Z. Iftikhar, A. Anthore, A. K. Mitchell, F. D. Parmentier, U. Gennser, A. Ouerghi, A. Cavanna, C. Mora, P. Simon, and F. Pierre, Tunable quantum criticality and super-ballistic transport in a “charge” kondo circuit, *Science* **360**, 1315 (2018), <https://www.science.org/doi/pdf/10.1126/science.aan5592>.
- [20] Z. Iftikhar, S. Jezouin, A. Anthore, U. Gennser, F. D. Parmentier, A. Cavanna, and F. Pierre, Two-channel kondo effect and renormalization flow with macroscopic quantum charge states, *Nature* **526**, 233 (2015).
- [21] J. M. Woodall, J. L. Freeouf, G. D. Pettit, T. Jackson, and P. Kirchner, Ohmic contacts to n-GaAs using graded band gap layers of Ga<sub>1-x</sub>In<sub>x</sub>As grown by molecular beam epitaxy, *Journal of Vacuum Science and Technology* **19**, 626 (1981), [eprint: https://pubs.aip.org/avs/jvst/article-pdf/19/3/626/11749673/626\\_1\\_online.pdf](https://pubs.aip.org/avs/jvst/article-pdf/19/3/626/11749673/626_1_online.pdf).
- [22] A. K. Mitchell, L. A. Landau, L. Fritz, and E. Sela, Universality and scaling in a charge two-channel kondo device, *Phys. Rev. Lett.* **116**, 157202 (2016).
- [23] O. Göktaş, *Small Alloyed Ohmic Contacts to 2DES and Sub-micron Scale Corbino Devices in Strong Magnetic Fields: Observation of a Zero Bias Anomaly and Single-Electron Charging*, Ph.D. thesis, Max Planck Institute for Solid State Research (2009), ph.D. Thesis.
- [24] C. L. Hsueh, P. Sriram, T. Wang, C. Thomas, G. Gardner, M. A. Kastner, M. J. Manfra, and D. Goldhaber-Gordon, Clean quantum point contacts in an inas quantum well grown on a lattice-mismatched inp substrate, *Physical Review B* **105**, 10.1103/PhysRevB.105.195303 (2022).
- [25] A. T. Hatke, T. Wang, C. Thomas, G. C. Gardner, and M. J. Manfra, Mobility in excess of 106 cm<sup>2</sup>/v s in inas quantum wells grown on lattice mismatched inp substrates, *Applied Physics Letters* **111**, 10.1063/1.4993784 (2017).
- [26] I. O. Kulik and R. I. Shekhter, *Kinetic phenomena and charge discreteness effects in granulated media*, Tech. Rep. (1975).
- [27] C. W. J. Beenakker, Theory of coulomb-blockade oscillations in the conductance of a quantum dot, *Phys. Rev. B* **44**, 1646 (1991).
- [28] A. Fuhrer, *Phase coherence, orbital and spin states in quantum rings*, Doctoral thesis, ETH Zurich, Zürich (2003), diss., Naturwissenschaften ETH Zürich, Nr. 15094, 2003.
- [29] L. Kouwenhoven and C. Marcus, Quantum dots, *Physics World* **11**, 35 (1998).
- [30] L. P. Kouwenhoven, D. G. Austing, and S. Tarucha, Few-electron quantum dots, *Reports on Progress in Physics* **64**, 701 (2001).
- [31] S. Jezouin, Z. Iftikhar, A. Anthore, F. D. Parmentier, U. Gennser, A. Cavanna, A. Ouerghi, I. P. Levkivskiy, E. Idrisov, E. V. Sukhorukov, L. I. Glazman, and F. Pierre, Controlling charge quantization with quantum fluctuations, *Nature* **536**, 58 (2016).
- [32] E. Paladino, Y. M. Galperin, G. Falci, and B. L. Altshuler,  $1/f$  noise: Implications for solid-state quantum information, *Rev. Mod. Phys.* **86**, 361 (2014).
- [33] S. Kogan, *Electronic Noise and Fluctuations in Solids* (Cambridge University Press, 1996).
- [34] W.-C. Hua, M. Lee, P. Chen, M.-J. Tsai, and C. Liu, Threading dislocation induced low frequency noise in strained-si nmos-fets, *IEEE Electron Device Letters* **26**, 667 (2005).
- [35] F. Liefink, J. I. Dijkhuis, and H. van Houten, Low-frequency noise in quantum point contacts, *Semiconductor Science and Technology* **9**, 2178 (1994).
- [36] G. Ramon and X. Hu, Decoherence of spin qubits due to a nearby charge fluctuator in gate-defined double dots, *Phys. Rev. B* **81**, 045304 (2010).
- [37] C. Dekker, A. J. Scholten, F. Liefink, R. Eppenga, H. van Houten, and C. T. Foxon, Spontaneous resistance switching and low-frequency noise in quantum point contacts, *Phys. Rev. Lett.* **66**, 2148 (1991).
- [38] M. Pioro-Ladrière, J. H. Davies, A. R. Long, A. S. Sachrajda, L. Gaudreau, P. Zawadzki, J. Lapointe, J. Gupta, Z. Wasilewski, and S. Studenikin, Origin of switching noise in GaAs/al<sub>x</sub>ga<sub>1-x</sub>As lateral gated devices, *Phys. Rev. B* **72**, 115331 (2005).
- [39] D. H. Cobden, A. Savchenko, M. Pepper, N. K. Patel, D. A. Ritchie, J. E. F. Frost, and G. A. C. Jones, Time-irreversible random telegraph signal due to current along a single hopping chain, *Phys. Rev. Lett.* **69**, 502 (1992).
- [40] J. Smith, C. Berven, M. Wybourne, and S. Goodnick, Conductance instabilities in quantum point contacts, *Surface Science* **361-362**, 656 (1996).
- [41] S. Diehl, A. Micheli, A. Kantian, B. Kraus, H. P. Büchler, and P. Zoller, Quantum states and phases in driven open quantum systems with cold atoms, *Nature Physics* **4**, 878 (2008).
- [42] L. Viola, E. Knill, and S. Lloyd, Dynamical decoupling of open quantum systems, *Phys. Rev. Lett.* **82**, 2417 (1999).
- [43] M. J. Biercuk, H. Uys, A. P. VanDevender, N. Shiga, W. M. Itano, and J. J. Bollinger, Optimized dynamical decoupling in a model quantum memory, *Nature* **458**, 996 (2009).
- [44] E. J. Connors, J. Nelson, H. Qiao, L. F. Edge, and J. M. Nichol, Low-frequency charge noise in si/sige quantum dots, *Phys. Rev. B* **100**, 165305 (2019).
- [45] R. H. Kingston, ed., *Semiconductor Surface Physics* (Literary Licensing, LLC, United States, 2012) reprint of the 1957 edition; with contributions from Elias Burstein and A. L. McWhorter.
- [46] P. Dutta and P. M. Horn, Low-frequency fluctuations in solids:  $\frac{1}{f}$  noise, *Rev. Mod. Phys.* **53**, 497 (1981).
- [47] B. Paquelet Wuetz, D. Degli Esposti, A.-M. J. Zwerver, S. V. Amitonov, M. Botifoll, J. Arbiol, A. Sammak, L. M. K. Vandersypen, M. Russ, and G. Scappucci, Reducing charge noise in quantum dots by using thin silicon quantum wells, *Nature Communications* **14**, 1385 (2023).
- [48] L. Massai, B. Hetényi, M. Mergenthaler, F. J. Schupp, L. Sommer, S. Paredes, S. W. Bedell, P. Harvey-Collard, G. Salis, A. Fuhrer, and N. W. Hendrickx, Impact of interface traps on charge noise and low-density transport properties in Ge/SiGe heterostructures, *Communications Materials* **5**, 151 (2024).
- [49] E. J. Connors, J. Nelson, L. F. Edge, and J. M. Nichol, Charge-noise spectroscopy of Si/SiGe quantum dots via dynamically-decoupled exchange oscillations, *Nature Communications* **13**, 940 (2022).
- [50] J. Basset, A. Stockklauser, D.-D. Jarausch, T. Frey, C. Reichl, W. Wegscheider, A. Wallraff, K. Ensslin, and T. Ihn, Evaluating charge noise acting on semiconductor quantum dots in the circuit quantum electrodynamics architecture, *Applied Physics*

- Letters **105**, 063105 (2014).
- [51] F. Jekat, B. Pestka, D. Car, S. Gazibegović, K. Flöhr, S. Heedt, J. Schubert, M. Liebmann, E. P. A. M. Bakkers, T. Schäpers, and M. Morgenstern, Exfoliated hexagonal BN as gate dielectric for InSb nanowire quantum dots with improved gate hysteresis and charge noise, *Applied Physics Letters* **116**, 253101 (2020), eprint: [https://pubs.aip.org/aip/apl/article-pdf/doi/10.1063/5.0002112/13174099/253101\\_1\\_online.pdf](https://pubs.aip.org/aip/apl/article-pdf/doi/10.1063/5.0002112/13174099/253101_1_online.pdf).
  - [52] X. Mi, S. Kohler, and J. R. Petta, Landau-zener interferometry of valley-orbit states in si/sige double quantum dots, *Phys. Rev. B* **98**, 161404 (2018).
  - [53] K. D. Petersson, J. R. Petta, H. Lu, and A. C. Gossard, Quantum coherence in a one-electron semiconductor charge qubit, *Phys. Rev. Lett.* **105**, 246804 (2010).
  - [54] P. Huang and X. Hu, Spin relaxation in a si quantum dot due to spin-valley mixing, *Phys. Rev. B* **90**, 235315 (2014).
  - [55] P. Huang and X. Hu, Electron spin relaxation due to charge noise, *Physical Review B - Condensed Matter and Materials Physics* **89**, 10.1103/PhysRevB.89.195302 (2014).
  - [56] L. P. Kouwenhoven, N. C. van der Vaart, A. T. Johnson, W. Kool, C. J. P. M. Harmans, J. G. Williamson, A. A. M. Staring, and C. T. Foxon, Single electron charging effects in semiconductor quantum dots, *Zeitschrift für Physik B Condensed Matter* **85**, 367 (1991).
  - [57] S. Amasha, I. G. Rau, M. Grobis, R. M. Potok, H. Shtrikman, and D. Goldhaber-Gordon, Coulomb blockade in an open quantum dot, *Phys. Rev. Lett.* **107**, 216804 (2011).
  - [58] D. Berman, N. B. Zhitenev, R. C. Ashoori, and M. Shayegan, Observation of quantum fluctuations of charge on a quantum dot, *Phys. Rev. Lett.* **82**, 161 (1999).
  - [59] D. Chouvaev, L. S. Kuzmin, D. S. Golubev, and A. D. Zaikin, Strong tunneling and coulomb blockade in a single-electron transistor, *Phys. Rev. B* **59**, 10599 (1999).
  - [60] P. Joyez, V. Bouchiat, D. Esteve, C. Urbina, and M. H. Devoret, Strong tunneling in the single-electron transistor, *Phys. Rev. Lett.* **79**, 1349 (1997).
  - [61] A. Staring, J. Williamson, H. van Houten, C. Beenakker, L. Kouwenhoven, and C. Foxon, Coulomb-blockade oscillations in a quantum dot, *Physica B: Condensed Matter* **175**, 226 (1991), analogies in Optics and Micro-Electronics.
  - [62] A. Furusaki and K. A. Matveev, Theory of strong inelastic cotunneling, *Phys. Rev. B* **52**, 16676 (1995).
  - [63] H. Yi and C. L. Kane, Coulomb blockade in a quantum dot coupled strongly to a lead, *Phys. Rev. B* **53**, 12956 (1996).
  - [64] F. D. Parmentier, A. Anthore, S. Jezouin, H. le Sueur, U. Gennser, A. Cavanna, D. Mailly, and F. Pierre, Strong back-action of a linear circuit on a single electronic quantum channel, *Nature Physics* **7**, 935 (2011).
  - [65] K. Flensberg, Capacitance and conductance of mesoscopic systems connected by quantum point contacts, *Phys. Rev. B* **48**, 11156 (1993).
  - [66] K. Flensberg, S. Girvin, M. Jonson, D. Penn, and M. Stiles, Coulomb blockade in single tunnel-junctions: Quantum mechanical effects of the electromagnetic environment, (1991).
  - [67] P. Joyez, D. Esteve, and M. H. Devoret, How is the coulomb blockade suppressed in high-conductance tunnel junctions?, *Phys. Rev. Lett.* **80**, 1956 (1998).
  - [68] G.-L. Ingold and Y. V. Nazarov, Charge tunneling rates in ultra-small junctions, *arXiv preprint cond-mat/0508728* (2005).
  - [69] M. Kindermann and Y. V. Nazarov, Interaction effects on counting statistics and the transmission distribution, *Phys. Rev. Lett.* **91**, 136802 (2003).
  - [70] S. Doniach, The kondo lattice and weak antiferromagnetism, *Physica B+C* **91**, 231 (1977).
  - [71] P. Coleman, Heavy fermions and the kondo lattice: A 21st century perspective, in *Many-Body Physics: From Kondo to Hubbard*, Schriften des Forschungszentrums Jülich: Modeling and Simulation, Vol. 5, edited by E. Pavarini, E. Koch, and P. Coleman (Forschungszentrum Jülich GmbH, Zentralbibliothek, Verlag, 2015) pp. 1.1–1.34.
  - [72] S. Steiger, M. Povolotskyi, H.-H. Park, T. Kubis, and G. Klimeck, Nemo5: A parallel multiscale nanoelectronics modeling tool, *IEEE Transactions on Nanotechnology* **10**, 1464 (2011).
  - [73] S. D. Sarma and E. H. Hwang, Universal density scaling of disorder-limited low-temperature conductivity in high-mobility two-dimensional systems, *Physical Review B* **88**, 035439 (2013).
  - [74] S. Datta, *Electronic Transport in Mesoscopic Systems* (Cambridge University Press, Cambridge, UK, 1995).
  - [75] L. E. A. Stehouwer, C. X. Yu, B. van Straaten, A. Tosato, V. John, D. Degli Esposti, A. Elsayed, D. Costa, S. D. Oosterhout, N. W. Hendrickx, M. Veldhorst, F. Borsoi, and G. Scappucci, Exploiting strained epitaxial germanium for scaling low-noise spin qubits at the micrometre scale, *Nature Materials* **10.1038/s41563-025-02276-w** (2025).



# Supplemental Material: Hybrid metal-semiconductor quantum dots in InAs as a platform for quantum simulation

## S1. INDIUM ARSENIDE QUANTUM WELL HETEROSTRUCTURE STACK

A cross-sectional schematic of the InAs quantum well (QW) layer structure is shown in Fig. S1(a). The 4 nm InAs QW sandwiched between 10.5 nm  $\text{In}_{0.75}\text{Ga}_{0.25}\text{As}$  barriers forms the active region of the stack and hosts the two-dimensional electron gas (2DEG). Self-consistent Schrödinger-Poisson simulations with NEMO5[72] (see Fig. S1(d)) reveal an electron density concentrated in the InAs QW, with a single subband occupied. The 2DEG electron density extracted from low-field Hall resistance and Shubnikov-de Haas (SdH) oscillations in a 60  $\mu\text{m}$  wide ungated Hall-bar fabricated on the same chip corroborate the occupation of a single subband, with density  $n_{\text{Hall}} \simeq n_{\text{SdH}} = 4.81 \times 10^{11} \text{ cm}^{-2}$  and a mobility of  $\mu = 6.4 \times 10^5 \text{ cm}^2/\text{Vs}$  (see Fig. S1(b)).

The mobility variation with density is probed on a nominally identical Hall-bar with a Ti/Au top gate to tune the density. The linear dependence of the density on the top gate voltage, expected from a simple capacitive model, is depicted in Fig. S1(c), with the mobility dependence on density shown in Fig. S1(e). A fit to a  $\mu \propto n^\alpha$  power law in the Thomas-Fermi screening limit yields  $\alpha = 0.5$ , consistent with mobility limited by unintentional background impurities and native charged point defects[73].

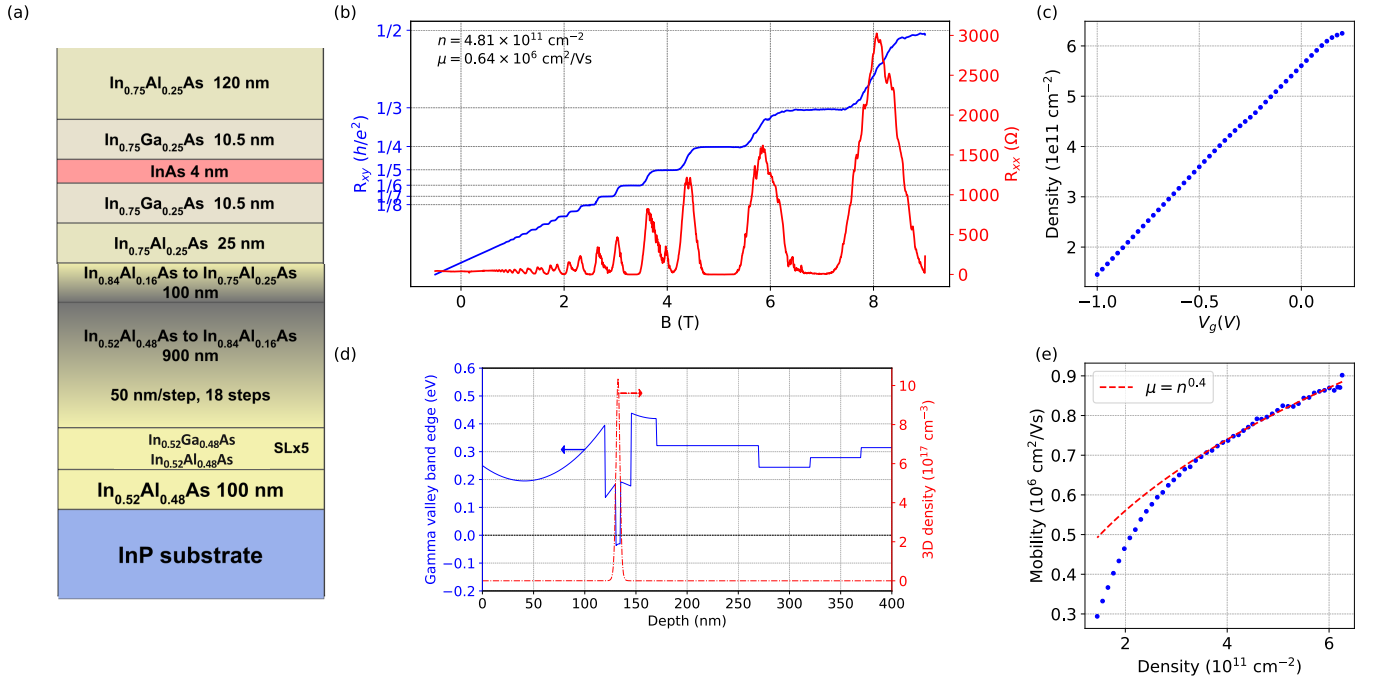


FIG. S1. (a) Cross-sectional schematic showing the layer structure of the InAs heterostructure stack. (b) Four-terminal magnetotransport data for a 60  $\mu\text{m}$  wide ungated Hall-bar. (c) Density modulation on a different Hall-bar device with a Ti/Au gate biased at  $V_g$ . The linear dependence of density on voltage is expected from a simple capacitance model. (d)  $\Gamma$ -valley conduction band edge and electron density of the quantum well from a self-consistent 1D Schrödinger-Poisson simulation using NEMO5. The energy scale in (d) is referenced to the Fermi level. (e) Mobility variation with density, with a  $\mu \propto n^{0.4}$  power law fit to the data. See text for discussion.

## S2. ADDITIONAL FABRICATION DETAILS

Electron-beam lithography was performed at the Stanford Nano Shared Facilities with a 50 kV Raith Voyager using 495k PMMA A5 resist and developed in 1:3 methyl isobutyl ketone (MIBK): isopropanol. Resist removal was aided by a remote oxygen plasma descumming step. The wet mesa etchant comprised 12.01 g of citric acid anhydrous in solution with 250 mL  $\text{H}_2\text{O}$ , 3 mL  $\text{H}_3\text{PO}_4$  (85%), and 3 mL  $\text{H}_2\text{O}_2$  (30%). The etch depth of 400 nm was chosen to avoid parallel conduction in the buffer layer which had been observed in similar heterostructures but not necessarily this one. In the ohmic contact step, following the mask development the sample was dipped in a dilute (1:9) solution of HCl to remove native oxide on the exposed InAs sidewalls. The 35-nm  $\text{HfO}_2$  dielectric layer was grown by thermal ALD at 150°C using a Cambridge Nanotech (now Veeco) Savannah.

### S3. INSTRUMENTATION AND MEASUREMENT DETAILS

Current biased transport measurement were performed as shown in the schematic of the measurement setup in Fig. 1 of the main text. A low frequency ( $< 100$  Hz) AC 50 mV - 1 V RMS sinusoidal signal was sourced from a Stanford Research Systems SR860 lock-in amplifier with a  $100\text{ M}\Omega$  bias resistor. The variable DC bias current  $I_{\text{bias}}$  was provided by a Quantum Machines QDAC voltage source with another  $100\text{ M}\Omega$  bias resistor. The AC and DC bias currents were summed connected to the source terminal of the devices, and drained at both ends of the island through grounded contacts that were tied directly to the cold finger of the dilution refrigerator. The voltage drop between voltage probes downstream of the island and the grounded current drain was amplified by a factor of 100 using an NF SA-240F5 low noise FET preamplifier. The AC output of the preamplifier,  $V_{\text{S,R,T,I}}$ , was measured using a Stanford Research Systems SR830 lock-in amplifier, and the DC output was measured using a Keysight 34465A digital multimeter. The QPC and plunger gate voltages were sourced from a Quantum Machines QDAC.

### S4. LANDAUER-BUTTIKER ANALYSIS OF QUANTUM HALL EDGE STATE TRANSPARENCY

#### A. Derivation of Device Conductance in Quantum Hall

In the following section, we derive equations 1 and 2 in the main text using a Landauer Buttiker analysis. To simplify our analysis, we use a modified diagram shown below in Figure S2, whose layout of ohmics is identical to the device shown in Figure 2 of the main text, but which has the ohmics labelled for convenience.

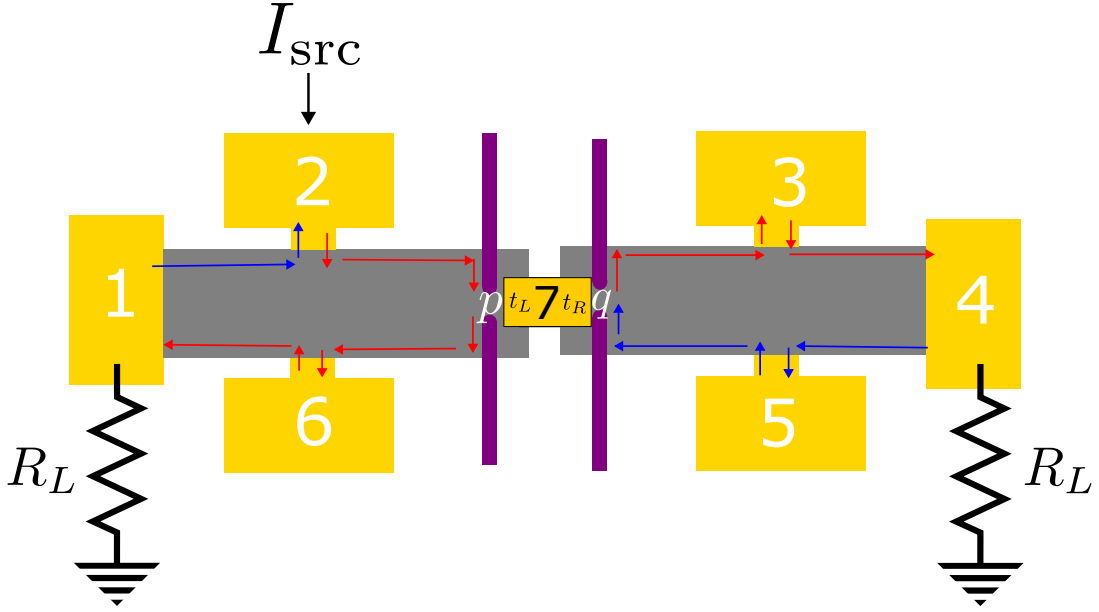


FIG. S2. Device schematic. Current  $I_{\text{src}}$  is sourced at 2, and drained at 1 and 4 via a line resistance  $R_L$ . A clockwise chirality of the edge states is assumed.

For a derivation of equation 1, we begin by neglecting the details of the edge state transparency through the island, and derive the conductance through the entire device as a function of the voltages measured on each terminal.

The following calculation is done based on the formalism described in [74].

$$G_{x \leftarrow y} = G_0 \times \begin{matrix} & \begin{matrix} 1 & 2 & 3 & 4 & 5 & 6 \end{matrix} \\ \begin{matrix} 1 \\ 2 \\ 3 \\ 4 \\ 5 \\ 6 \end{matrix} & \begin{pmatrix} 0 & 0 & 0 & 0 & 0 & 1 \\ 1 & 0 & 0 & 0 & 0 & 0 \\ 0 & G_{32} & 0 & 0 & G_{35} & 0 \\ 0 & 0 & 1 & 0 & 0 & 0 \\ 0 & 0 & 0 & 1 & 0 & 0 \\ 0 & G_{62} & 0 & 0 & G_{65} & 0 \end{pmatrix} \end{matrix}, \quad (\text{S1})$$

Here, we note that  $G_0 = \nu \frac{e^2}{h}$  is the longitudinal quantum hall conductance, and

$$\begin{aligned} G_{32} &= \frac{G_{\text{device}}}{G_0} = \alpha \\ G_{35} &= \frac{G_0 - G_{\text{device}}}{G_0} = 1 - \alpha \\ G_{62} &= \frac{G_0 - G_{\text{device}}}{G_0} = 1 - \alpha \\ G_{65} &= \frac{G_{\text{device}}}{G_0} = \alpha \end{aligned}$$

These coefficients  $G_{32}$  and  $G_{65}$  represent the device conductance, whereas the other formulas can be derived from properties of the conductance matrix  $\sum_y G_{x \leftarrow y} = G_0$ . We now can invoke the Buttiker formula

$$I_x = \sum_y [G_{yx} V_x - G_{xy} V_y] \quad (\text{S2})$$

In addition to  $\sum_y G_{x \leftarrow y} = G_0$ , we also know  $\sum_x G_{x \leftarrow y} = G_0$ , so we can write

$$\begin{aligned} I_x &= \sum_y [G_{yx} V_x - G_{xy} V_y] \\ I_x &= G_0 V_x - \sum_y [G_{xy} V_y] \\ &= \sum_y [(G_0 \delta_{xy} - G_{xy}) V_y] \end{aligned}$$

$$\begin{pmatrix} I_1 \\ I_2 \\ I_3 \\ I_4 \\ I_5 \\ I_6 \end{pmatrix} = G_0 \begin{pmatrix} 1 & 0 & 0 & 0 & 0 & -1 \\ -1 & 1 & 0 & 0 & 0 & 0 \\ 0 & -\alpha & 1 & 0 & \alpha - 1 & 0 \\ 0 & 0 & -1 & 1 & 0 & 0 \\ 0 & 0 & 0 & -1 & 1 & 0 \\ 0 & \alpha - 1 & 0 & 0 & -\alpha & 1 \end{pmatrix} \begin{pmatrix} V_1 \\ V_2 \\ V_3 \\ V_4 \\ V_5 \\ V_6 \end{pmatrix} \quad (\text{S3})$$

We further note that

$$\begin{pmatrix} I_1 \\ I_2 \\ I_3 \\ I_4 \\ I_5 \\ I_6 \end{pmatrix} = \begin{pmatrix} -V_1/R_L \\ I_{\text{src}} \\ 0 \\ -V_4/R_L \\ 0 \\ 0 \end{pmatrix} = \begin{pmatrix} -G_0 \frac{V_1}{\delta} \\ I_{\text{src}} \\ 0 \\ -G_0 \frac{V_4}{\delta} \\ 0 \\ 0 \end{pmatrix},$$

since contacts 1 and 4 are grounded with line resistance  $R_L$ , contact 2 has a source current  $I_{\text{src}}$ , and all other contacts are floating. Here,  $\delta = R_L G_0$  is a dimensionless line resistance. We have

$$\begin{aligned}
& -G_0 \begin{pmatrix} \frac{1}{\delta} & 0 & 0 & 0 & 0 & 0 \\ 0 & 0 & 0 & 0 & 0 & 0 \\ 0 & 0 & 0 & 0 & 0 & 0 \\ 0 & 0 & 0 & \frac{1}{\delta} & 0 & 0 \\ 0 & 0 & 0 & 0 & 0 & 0 \\ 0 & 0 & 0 & 0 & 0 & 0 \end{pmatrix} \begin{pmatrix} V_1 \\ V_2 \\ V_3 \\ V_4 \\ V_5 \\ V_6 \end{pmatrix} + \begin{pmatrix} 0 \\ I_{\text{src}} \\ 0 \\ 0 \\ 0 \\ 0 \end{pmatrix} = G_0 \begin{pmatrix} 1 & 0 & 0 & 0 & 0 & -1 \\ -1 & 1 & 0 & 0 & 0 & 0 \\ 0 & -\alpha & 1 & 0 & \alpha-1 & 0 \\ 0 & 0 & -1 & 1 & 0 & 0 \\ 0 & 0 & 0 & -1 & 1 & 0 \\ 0 & \alpha-1 & 0 & 0 & -\alpha & 1 \end{pmatrix} \begin{pmatrix} V_1 \\ V_2 \\ V_3 \\ V_4 \\ V_5 \\ V_6 \end{pmatrix} \\
& \begin{pmatrix} 0 \\ I_{\text{src}} \\ 0 \\ 0 \\ 0 \\ 0 \end{pmatrix} = G_0 \begin{pmatrix} 1+\frac{1}{\delta} & 0 & 0 & 0 & 0 & -1 \\ -1 & 1 & 0 & 0 & 0 & 0 \\ 0 & -\alpha & 1 & 0 & \alpha-1 & 0 \\ 0 & 0 & -1 & 1+\frac{1}{\delta} & 0 & 0 \\ 0 & 0 & 0 & -1 & 1 & 0 \\ 0 & \alpha-1 & 0 & 0 & -\alpha & 1 \end{pmatrix} \begin{pmatrix} V_1 \\ V_2 \\ V_3 \\ V_4 \\ V_5 \\ V_6 \end{pmatrix} \\
& G_0^{-1} \begin{pmatrix} 1+\frac{1}{\delta} & 0 & 0 & 0 & 0 & -1 \\ -1 & 1 & 0 & 0 & 0 & 0 \\ 0 & -\alpha & 1 & 0 & \alpha-1 & 0 \\ 0 & 0 & -1 & 1+\frac{1}{\delta} & 0 & 0 \\ 0 & 0 & 0 & -1 & 1 & 0 \\ 0 & \alpha-1 & 0 & 0 & -\alpha & 1 \end{pmatrix}^{-1} \begin{pmatrix} 0 \\ I_{\text{src}} \\ 0 \\ 0 \\ 0 \\ 0 \end{pmatrix} = \begin{pmatrix} V_1 \\ V_2 \\ V_3 \\ V_4 \\ V_5 \\ V_6 \end{pmatrix}
\end{aligned}$$

The solutions are, for the case of  $\delta = 0$ , are given by

$$\begin{aligned}
V_1 &= \frac{\delta + \alpha(\delta - 1)\delta}{G_0(1 + 2\alpha\delta)} I_{\text{src}} = 0 \\
V_2 &= \frac{(1 + \delta)(1 + \alpha\delta)}{G_0(1 + 2\alpha\delta)} I_{\text{src}} = \frac{I_{\text{src}}}{G_0} \\
V_3 &= \frac{\alpha(1 + \delta)^2}{G_0(1 + 2\alpha\delta)} I_{\text{src}} = \frac{\alpha I_{\text{src}}}{G_0} \\
V_4 &= \frac{\alpha\delta(1 + \delta)}{G_0(1 + 2\alpha\delta)} I_{\text{src}} = 0 \\
V_5 &= V_4 = 0 \\
V_6 &= \frac{1 - \alpha + \delta + \alpha\delta^2}{G_0(1 + 2\alpha\delta)} I_{\text{src}} = \frac{(1 - \alpha)I_{\text{src}}}{G_0}
\end{aligned}$$

Thus,

$$\alpha = \frac{V_3}{V_3 + V_6}$$

remembering that  $\alpha = \frac{G_{\text{device}}}{G_0}$ , with  $G_0 = v \frac{e^2}{h}$ , identifying the transmitted voltage  $V_T = V_3$ , and reflected voltage  $V_R = V_6$ , we arrive at equation 1 from the main text

$$G_{\text{device}} = v \frac{e^2}{h} \frac{V_T}{V_T + V_R}.$$

## B. Landauer Buttiker analysis of island transparency

We now perform an Landauer Buttiker analysis to determine the transparencies of the small metal island in ohmic contact with the semiconductor. Because the island acts as a small ohmic contact, the full treatment that allows us to separate independently

the right and left interfaces necessitates a 7x7 matrix, instead of the 6x6 matrix above.

$$G_{x \leftarrow y} = G_0 \times \begin{matrix} & \begin{matrix} 1 & 2 & 3 & 4 & 5 & 6 & 7 \end{matrix} \\ \begin{matrix} 1 \\ 2 \\ 3 \\ 4 \\ 5 \\ 6 \\ 7 \end{matrix} & \begin{pmatrix} 0 & 0 & 0 & 0 & 0 & 1 & 0 \\ 1 & 0 & 0 & 0 & 0 & 0 & 0 \\ 0 & 0 & 0 & 0 & G_{35} & 0 & G_{37} \\ 0 & 0 & 1 & 0 & 0 & 0 & 0 \\ 0 & 0 & 0 & 1 & 0 & 0 & 0 \\ 0 & G_{62} & 0 & 0 & 0 & 0 & G_{67} \\ 0 & G_{72} & 0 & 0 & G_{75} & 0 & G_{77} \end{pmatrix} \end{matrix}, \quad (S4)$$

where  $G_0 = v_0 e^2 / h$  for bulk filling factor  $v_0$ , and

$$G_{35} = (1 - q) + q(1 - t_R) = 1 - qt_R \quad (S5)$$

$$G_{37} = qt_R \quad (S6)$$

$$G_{62} = (1 - p) + p(1 - t_L) = 1 - pt_L \quad (S7)$$

$$G_{67} = pt_L \quad (S8)$$

$$G_{72} = pt_L \quad (S9)$$

$$G_{75} = qt_R \quad (S10)$$

Here  $p, q = v_{1,2}/v_0$  is the ratio of local filling factor to bulk filling factor in QPCs 1 and 2 respectively, and  $t_{L,R}$  is the mean transparency of the island to edge states on the left and right side respectively. We can invoke equation S4 B and a similar analysis to above, we have

$$I_x = \sum_y [G_{yx} V_x - G_{xy} V_y]$$

$$\begin{aligned} \begin{pmatrix} I_1 \\ I_2 \\ 0 \\ I_4 \\ 0 \\ 0 \\ 0 \end{pmatrix} &= G_0 \times \begin{pmatrix} 1 & 0 & 0 & 0 & 0 & -1 & 0 \\ -1 & 1 & 0 & 0 & 0 & 0 & 0 \\ 0 & 0 & 1 & 0 & -G_{35} & 0 & -G_{37} \\ 0 & 0 & -1 & 1 & 0 & 0 & 0 \\ 0 & 0 & 0 & -1 & 1 & 0 & 0 \\ 0 & -G_{62} & 0 & 0 & 0 & 1 & -G_{67} \\ 0 & -G_{72} & 0 & 0 & -G_{75} & 0 & G_{72} + G_{75} \end{pmatrix} \begin{pmatrix} V_1 \\ V_2 \\ V_3 \\ V_4 \\ V_5 \\ V_6 \\ V_7 \end{pmatrix} \\ &= G_0 \times \begin{pmatrix} 1 & 0 & 0 & 0 & 0 & -1 & 0 \\ -1 & 1 & 0 & 0 & 0 & 0 & 0 \\ 0 & 0 & 1 & 0 & qt_R - 1 & 0 & -qt_R \\ 0 & 0 & -1 & 1 & 0 & 0 & 0 \\ 0 & 0 & 0 & -1 & 1 & 0 & 0 \\ 0 & pt_L - 1 & 0 & 0 & 0 & 1 & -pt_L \\ 0 & -pt_L & 0 & 0 & -qt_R & 0 & pt_L + qt_R \end{pmatrix} \begin{pmatrix} V_1 \\ V_2 \\ V_3 \\ V_4 \\ V_5 \\ V_6 \\ V_7 \end{pmatrix}, \end{aligned}$$

where again we have used  $I_{3,5,6,7} = 0$  for floating contacts. Similarly to above, we can relate the current at the drains to the dimensionless line resistance  $\delta = R_L G_0$

$$I_{1,4} = -V_{1,4}/R_L = -G_0 \frac{V_{1,4}}{\delta}, \quad (S11)$$

where the current is positive for current flowing into the device. Just as above, we have a current  $I_{src}$  sourced at contact 2.

$$\begin{aligned}
-G_0 \begin{pmatrix} \frac{1}{\delta} & 0 & 0 & 0 & 0 & 0 \\ 0 & 0 & 0 & 0 & 0 & 0 \\ 0 & 0 & 0 & 0 & 0 & 0 \\ 0 & 0 & 0 & \frac{1}{\delta} & 0 & 0 \\ 0 & 0 & 0 & 0 & 0 & 0 \\ 0 & 0 & 0 & 0 & 0 & 0 \end{pmatrix} \begin{pmatrix} V_1 \\ V_2 \\ V_3 \\ V_4 \\ V_5 \\ V_6 \end{pmatrix} + \begin{pmatrix} 0 \\ I_{\text{src}} \\ 0 \\ 0 \\ 0 \\ 0 \end{pmatrix} &= G_0 \begin{pmatrix} 1 & 0 & 0 & 0 & 0 & -1 & 0 \\ -1 & 1 & 0 & 0 & 0 & 0 & 0 \\ 0 & 0 & 1 & 0 & qt_R - 1 & 0 & -qt_R \\ 0 & 0 & -1 & 1 & 0 & 0 & 0 \\ 0 & 0 & 0 & -1 & 1 & 0 & 0 \\ 0 & pt_L - 1 & 0 & 0 & 0 & 1 & -pt_L \\ 0 & -pt_L & 0 & 0 & -qt_R & 0 & pt_L + qt_R \end{pmatrix} \begin{pmatrix} V_1 \\ V_2 \\ V_3 \\ V_4 \\ V_5 \\ V_6 \end{pmatrix} \\
\begin{pmatrix} 0 \\ I_{\text{src}} \\ 0 \\ 0 \\ 0 \\ 0 \end{pmatrix} &= G_0 \begin{pmatrix} 1 + \frac{1}{\delta} & 0 & 0 & 0 & 0 & -1 & 0 \\ -1 & 1 & 0 & 0 & 0 & 0 & 0 \\ 0 & 0 & 1 & 0 & qt_R - 1 & 0 & -qt_R \\ 0 & 0 & -1 & 1 + \frac{1}{\delta} & 0 & 0 & 0 \\ 0 & 0 & 0 & -1 & 1 & 0 & 0 \\ 0 & pt_L - 1 & 0 & 0 & 0 & 1 & -pt_L \\ 0 & -pt_L & 0 & 0 & -qt_R & 0 & pt_L + qt_R \end{pmatrix} \begin{pmatrix} V_1 \\ V_2 \\ V_3 \\ V_4 \\ V_5 \\ V_6 \end{pmatrix} \\
\begin{pmatrix} V_1 \\ V_2 \\ V_3 \\ V_4 \\ V_5 \\ V_6 \end{pmatrix} &= G_0^{-1} \begin{pmatrix} 1 + \frac{1}{\delta} & 0 & 0 & 0 & 0 & -1 & 0 \\ -1 & 1 & 0 & 0 & 0 & 0 & 0 \\ 0 & 0 & 1 & 0 & qt_R - 1 & 0 & -qt_R \\ 0 & 0 & -1 & 1 + \frac{1}{\delta} & 0 & 0 & 0 \\ 0 & 0 & 0 & -1 & 1 & 0 & 0 \\ 0 & pt_L - 1 & 0 & 0 & 0 & 1 & -pt_L \\ 0 & -pt_L & 0 & 0 & -qt_R & 0 & pt_L + qt_R \end{pmatrix}^{-1} \begin{pmatrix} 0 \\ I_{\text{src}} \\ 0 \\ 0 \\ 0 \\ 0 \end{pmatrix}
\end{aligned}$$

$$\begin{aligned}
V_1 &= \frac{\delta(qt_R + p(t_L + (\delta - 1)qt_L t_R))}{G_0(qt_R + p(t_L + 2\delta qt_L t_R))} I_{\text{src}} \\
V_2 &= \frac{(\delta + 1)(qt_R + p(t_L + \delta qt_L t_R))}{G_0(qt_R + p(t_L + 2\delta qt_L t_R))} I_{\text{src}} \\
V_3 &= \frac{(1 + \delta)^2 pqt_L t_R}{G_0(qt_R + p(t_L + 2\delta qt_L t_R))} I_{\text{src}} \\
V_4 &= \frac{\delta(1 + \delta) pqt_L t_R}{G_0(qt_R + p(t_L + 2\delta qt_L t_R))} I_{\text{src}} \\
V_5 &= V_4 \\
V_6 &= \frac{(1 + \delta)(qt_R + p(t_L + (\delta - 1)qt_L t_R))}{G_0(qt_R + p(t_L + 2\delta qt_L t_R))} I_{\text{src}} \\
V_7 &= \frac{(1 + \delta)pt_L(1 + \delta qt_R)}{G_0(qt_R + p(t_L + 2\delta qt_L t_R))} I_{\text{src}}
\end{aligned}$$

If we consider the case of zero line resistance  $\delta = 0$ , we have

$$\begin{aligned}
V_2 &= \frac{I_{\text{src}}}{G_0} \\
V_1 &= 0 \\
V_3 &= \frac{pqt_L t_R}{G_0(qt_R + pt_L)} I_{\text{src}} \\
V_4 &= 0 \\
V_5 &= V_4 \\
V_6 &= \frac{(qt_R + pt_L - pqt_L t_R)}{G_0(qt_R + pt_L)} I_{\text{src}} \\
V_7 &= \frac{pt_L}{G_0(qt_R + pt_L)} I_{\text{src}}
\end{aligned}$$

Below, we show a table showing the transmitted voltage ratio  $V_3/V_2$  as a function of the filling factor ratio in each QPC  $q, p$  as a



function of the transparency (assuming symmetric interfaces such that  $t_L = t_R = t$ )

$q \downarrow, p \rightarrow$	0	1/4	1/3	1/2	2/3	3/4	1
0	0	0	0	0	0	0	0
1/4	0	$t/8$	—	$t/6$	—	$3t/16$	$t/5$
1/3	0	—	$t/6$	—	$2t/9$	—	$t/4$
1/2	0	$t/6$	—	$t/4$	—	$3t/10$	$t/3$
2/3	0	—	$2t/9$	—	$t/3$	—	$2t/5$
3/4	0	$3t/16$	—	$3t/10$	—	$3t/8$	$3t/7$
1	0	$t/5$	$t/4$	$t/3$	$2t/5$	$3t/7$	$t/2$

$$V_3/V_2 = \quad (S12)$$

$$V_6/V_2 = 1 - V_3/V_2 \quad (S13)$$

$q \downarrow, p \rightarrow$	0	1/4	1/3	1/2	2/3	3/4	1
0	—	1	1	1	1	1	1
1/4	0	1/2	—	2/3	—	3/4	4/5
1/3	0	—	1/2	—	2/3	—	3/4
1/2	0	1/3	—	1/2	—	3/5	2/3
2/3	0	—	1/3	—	1/2	—	3/5
3/4	0	1/4	—	2/5	—	1/2	4/7
1	0	1/5	1/4	1/3	2/5	3/7	1/2

$$V_7/V_2 = \quad (S14)$$

### C. Edge-state dependent transparency solutions

Especially at low quantum hall filling factors, when there can be a large spatial distributions of edge modes, the transparencies of the innermost quantum hall edge mode can often be significantly different from the outermost edge modes.

In order to calculate the individual transparencies of the edge modes, we can use the following prescription. When a QPC has filling factor ratio  $q, p = \frac{k}{v}$ , where  $k$  is the number of edge modes let through and  $v$  is the bulk filling factor, we can replace

$$pt_L \rightarrow p\overline{t_{v-k+1,L}}, qt_R \rightarrow q\overline{t_{v-k+1,R}}$$

with

$$\overline{t_{v-k+1,L}} = \frac{1}{k} \sum_{n=1}^k t_{n,L}$$

$$\overline{t_{v-k+1,R}} = \frac{1}{k} \sum_{n=1}^k t_{n,R}$$

i.e. we let  $k$  edge modes through the QPC, the transparency used in the Landauer-Buttiker formulas is the average of the  $k$  outer-most edge state transparencies.

If we set each QPC to transmit a single quantum hall edge mode (assuming symmetric interfaces such that  $t_{v,L} = t_{v,R} = t_v$ ), we derive equation 2 in the main text

$$\begin{aligned} \frac{V_6}{V_2} &= \frac{V_R^{\tau_{1,2}=1}}{V_R^{\tau_{1,2}=0}} \\ &= \frac{qt_{v,R} + pt_{v,L} - pqt_{v,L}t_{v,R}}{qt_{v,R} + pt_{v,L}} \\ &= \frac{t_v/v + t_v/v - t_v^2/v^2}{t_v/v + t_v/v} \\ &= 1 - \frac{t_v}{2v}. \end{aligned}$$

A more complicated case exists if we consider more than a single edge mode being allowed in one or both of the QPC. For example, if  $p = \frac{1}{3}$  and  $q = \frac{2}{3}$ , with  $v = 3$ , we have

$$\begin{aligned}\frac{V_3}{V_2} &= \left(\frac{1}{3}\right) \left(\frac{2}{3}\right) \frac{t_{3,L}\bar{t}_{2,R}}{(\frac{2}{3}\bar{t}_{2,R} + \frac{1}{3}t_{3,L})} \\ &= \frac{2}{3} \frac{t_{3,L}\bar{t}_{2,R}}{(2\bar{t}_{2,R} + t_{3,L})}, \quad \bar{t}_{2,R} = \frac{1}{2}(t_{3,R} + t_{2,R})\end{aligned}$$

Following this prescription, we display the results of similar calculations that yield edge-state dependent transparency solutions, for filling factors  $\nu = 2$  and  $\nu = 3$  as a function of the filling factor ratios in both QPCs  $p$  and  $q$ .

1.  $\nu = 2$

$$V_t/V_r^{\tau=0} = \begin{array}{c|c|c|c} q \downarrow, p \rightarrow & 0 & 1/2 & 1 \\ \hline 0 & 0 & 0 & 0 \\ 1/2 & 0 & t_{2,L}t_{2,R}/2(t_{2,L} + t_{2,R}) & \bar{t}_L\bar{t}_{2,R}/(2\bar{t}_L + t_{2,R}) \\ 1 & 0 & t_{2,L}\bar{t}_R/(t_{2,L} + 2\bar{t}_R) & \bar{t}_L\bar{t}_R/(\bar{t}_L + \bar{t}_R) \end{array}, \quad (\text{S15})$$

where

$$\begin{aligned}\bar{t}_L &= (t_{1,L} + t_{2,L})/2 \\ \bar{t}_R &= (t_{1,R} + t_{2,R})/2\end{aligned}$$

Assuming  $t_L = t_R$

$$V_t/V_s = \begin{array}{c|c|c|c} q \downarrow, p \rightarrow & 0 & 1/2 & 1 \\ \hline 0 & 0 & 0 & 0 \\ 1/2 & 0 & t_2/4 & \bar{t}t_2/(2\bar{t} + t_2) \\ 1 & 0 & t_2\bar{t}/(t_2 + 2\bar{t}) & \bar{t}/2 \end{array}, \quad (\text{S16})$$

where

$$\bar{t} = (t_2 + t_1)/2$$

2.  $\nu = 3$

$$V_3/V_2 = \begin{array}{c|c|c|c|c} q \downarrow, p \rightarrow & 0 & 1/3 & 2/3 & 1 \\ \hline 0 & 0 & 0 & 0 & 0 \\ 1/3 & 0 & t_{3,L}t_{3,R}/3(t_{3,L} + t_{3,R}) & 2t_{2,L}t_{3,R}/3(2\bar{t}_{2,L} + t_{3,R}) & \bar{t}_L t_{3,R}/(3\bar{t}_L + t_{3,R}) \\ 2/3 & 0 & 2t_{3,L}\bar{t}_{2,R}/3(t_{3,L} + 2\bar{t}_{2,R}) & 2t_{2,L}t_{2,R}/3(\bar{t}_{2,L} + t_{2,R}) & 2\bar{t}_L t_{2,R}/(3\bar{t}_L + 2\bar{t}_{2,R}) \\ 1 & 0 & t_{3,L}\bar{t}_R/(t_{3,L} + 3\bar{t}_R) & 2t_{2,L}\bar{t}_R/(2\bar{t}_{2,L} + 3\bar{t}_R) & \bar{t}_L\bar{t}_R/(\bar{t}_L + \bar{t}_R) \end{array}, \quad (\text{S17})$$

where

$$\begin{aligned}\bar{t}_L &= (t_{1,L} + t_{2,L} + t_{3,L})/3 \\ \bar{t}_R &= (t_{1,R} + t_{2,R} + t_{3,R})/3 \\ \bar{t}_{2,L} &= (t_{3,L} + t_{2,L})/2 \\ \bar{t}_{2,R} &= (t_{3,R} + t_{2,R})/2\end{aligned}$$

In order to read out the transparencies of each individual edge state, we perform a QPC-QPC megasweep, where we measure the transmitted and reflected voltages as a function of the two QPC voltages. When each QPC is transmitting 1 edge mode, we can read out the transparency of the outermost edge mode  $t_\nu$ . We can then open each QPC to two edge modes, and use our measured outermost edge transparency and the measure of the outer two most edge state average transparency  $\bar{t}_{\nu-1}$  to infer the transparency  $t_{\nu-1}$ . Each data point in Figure 2d in the main text represents a 2-dimensional dataset similar to what is shown in Figure 2b, where the diagonal elements  $p = q$  can be used to extract individual edge state transparencies.

## S5. FIELD-DEPENDENT EQUILIBRATION OF QUANTUM HALL EDGE MODES

The ability to inject a nonequilibrium distribution of edge mode electrochemical potentials through QPCs hinges on the assumption that the edge modes do not equilibrate over the 60  $\mu\text{m}$  distance between the QPC and the island in Device A. We can test this assumption by studying the extent of equilibration as a function of distance and magnetic field with the device depicted in Fig. S3(a). An *injector* QPC, nominally identical to the QPC in Device A, is tuned to the first conductance plateau, corresponding to transmission of only the outermost edge mode. A set of three *detector* QPCs are located adjacent to voltage probes at distances  $\ell \in \{0.7, 2.9, 5\} \mu\text{m}$  from the injector, and are tuned to transmit  $n \in \mathbb{Z} \leq \nu$  edge modes.

Assuming no equilibration among the edge modes over the distance between the injector and the first detector with  $n > 0$ , a Landauer-Büttiker treatment for electrochemical potential at the probe “ $i$ ” behind the detector QPC reads

$$\mu_d = \frac{1}{n} eV_S, \quad (\text{S18})$$

where  $eV_S$  is the electrochemical potential of the source contact “1” (see Fig. S3), upstream the injector QPC. Similarly, in the limit where  $m \leq \nu$  outer edge modes fully equilibrate before the detector QPC,  $\mu_d$  is given by

$$\mu_d = \begin{cases} (1/m)eV_S, & \text{if } n \leq m \\ (1/n)eV_S, & \text{if } n > m. \end{cases} \quad (\text{S19})$$

Comparing the voltage drop between the detector voltage probe “ $i$ ” and the current drain “6”,  $eV_d = \mu_d$ , with predictions from Eqs. S18 as a function of distance and magnetic field enables a quantitative study of edge mode equilibration. The measured four-terminal resistance  $R_{51,i6}$  for current flowing between contacts  $5 \leftarrow 1$  and voltage measured across  $i - 6$  where  $i \in \{2, 3, 4\}$  is shown in Fig. S3(b-g) together with predictions from Eqs. S18, S19 for three magnetic fields each on the  $\nu = 3, 4$  quantum Hall plateaus. The measured  $R_{51,i6}$  at  $\nu = 3$  is well explained by Eq. S18, indicating no equilibration between the edge modes over the longest distance  $\ell = 5 \mu\text{m}$ . In contrast, at the high field end of the  $\nu = 4$  quantum Hall plateau,  $R_{51,36}$  and  $R_{51,46}$  deviate from the predictions of Eq. S18 when the detector QPC is tuned to transmit only the outermost edge mode ( $n = 1$ ). This indicates partial equilibration between the outer two edge modes over distances greater than 700 nm. Although we cannot predict the extent of equilibration over the 60  $\mu\text{m}$  propagation length relevant for Device A, the results in this section indicate an equilibration length  $l_{\text{eq},\nu}$  that reduces with increasing field for a given  $\nu$ , and is shorter for  $\nu = 4$  (i.e.,  $l_{\text{eq},4} < l_{\text{eq},3}$ ). Further investigation of the  $l_{\text{eq},\nu}$  over longer injector-detector distances and higher filling factors is required to ascertain the role played by edge mode equilibration in the magnetic field and filling factor dependence of transparencies to submicron ohmic islands discussed in Sec. III of the main text.

## S6. DETAILS OF CHARGE NOISE SPECTROSCOPY

As mentioned in the main text, we use two distinct techniques to measure charge noise. For low-frequency charge noise, we use the Coulomb peak tracking method, and for high-frequency charge noise, we use the Coulomb flank method.

The Coulomb flank method has been used to collect charge noise measurements in the literature [44, 49, 75]. The Coulomb flank method involves performing a wide-bandwidth conductance measurement on the flank of a Coulomb peak, where the response of the quantum dot is most sensitive to the fluctuations in the local electrochemical potential. We use a low-frequency lock-in technique to measure the charge noise while filtering out high-frequency Johnson noise present in the setup above. We directly measure the time-series conductance data using the buffer of the SR860 lock-in, which can then be converted to a noise spectrum in the island chemical potential  $S_\mu$  using equation 5.

To perform wide-bandwidth lock-in measurements, we adjust the time constant of the lock-in such that the 3 decibel bandwidth of the low-pass filter after down-conversion filters out the down-converted harmonics of the lock-in frequency, as well as the high-frequency setup noise above 100 Hz. The 3-decibel bandwidth of the Gaussian FIR filters that we use is given by

$$f_{3\text{db}} = \frac{1.5}{2\pi t_c}. \quad (\text{S20})$$

For our SR860 lock-in amplifiers, a time constant of 3 ms corresponds to a 3 decibel bandwidth  $f_{3\text{dB}} = 80 \text{ Hz}$ . We use a lock-in frequency  $f_{\text{lo}} = 88 \text{ Hz}$ , such that the down-converted second harmonic of the lock-in signal is well outside the 3-dB bandwidth of the lock-in filters, and save the lock-in amplifier output to a buffer that samples the output at a rate  $f_s = 300 \text{ Hz}$ . We take data on the flank of the Coulomb peaks for a sample time  $t_s = 1000 \text{ s}$ .

After each trace, we re-tune our plunger gate voltage to remain on the flank of a Coulomb peak by performing a single-shot measurement for a range of gate voltages around the previous flank location. We perform these single-shot measurements at

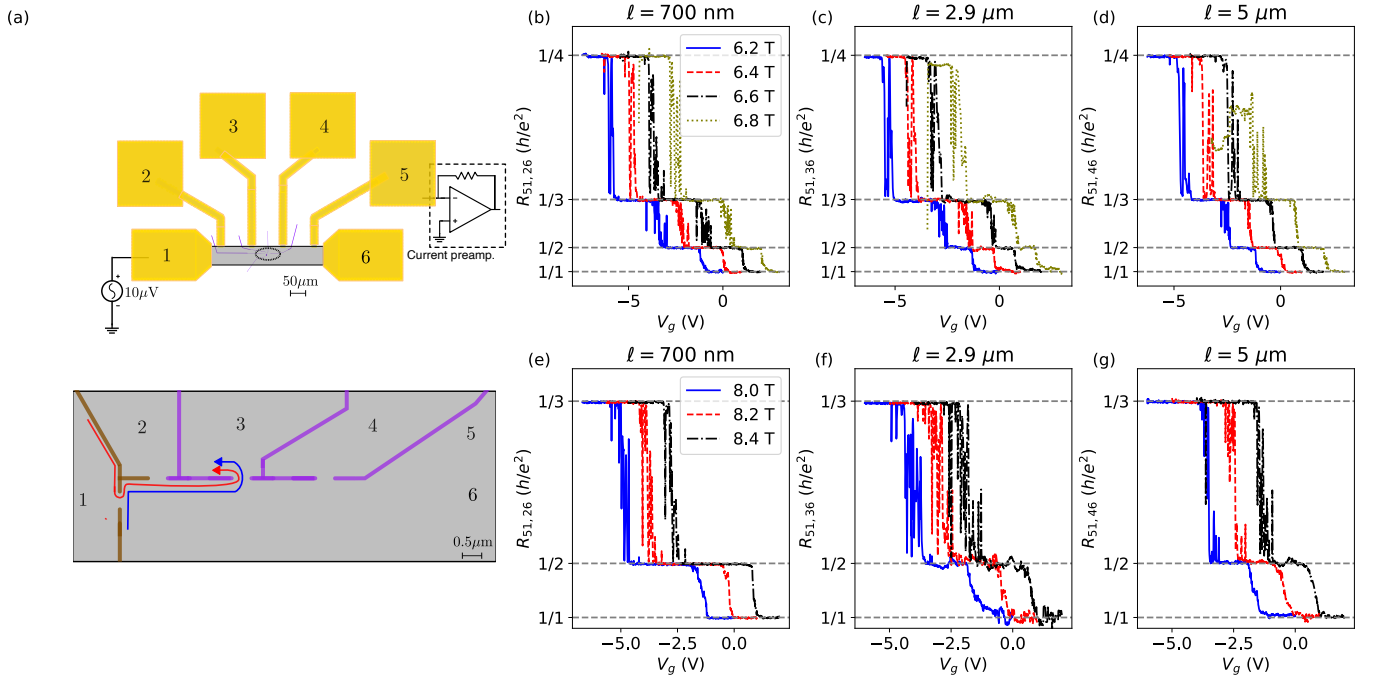


FIG. S3. **Quantum Hall equilibration length** (a) Device schematic for measuring quantum Hall equilibration and the measurement setup. The device features a 60  $\mu\text{m}$ -wide mesa (gray) with Ti/Au ohmic contacts (yellow), with quantum point contacts (dashed outline, expanded in the bottom panel) used for injecting and detecting a nonequilibrium distribution of electrochemical potentials. The injector (brown) is biased to the first conductance plateau to fully transmit the outermost edge mode, while the detectors (purple) are swept to measure the average electrochemical potential over an integer number of edge modes. The device is biased with a 10  $\mu\text{V}$  low-frequency ( $< 20$  Hz) ac excitation. The voltage drop between contacts  $i$  and 6 for  $i \in \{2, 3, 4\}$  across the corresponding detector QPC is measured after differential amplification by a lock-in amplifier. The detector QPCs are placed  $\ell = \{0.7, 2.9, 5\}$   $\mu\text{m}$  from the injector. A current preamplifier provides a virtual ground at the drain contact 5, and a lock-in amplifier is used to measure the drain current. (b)-(d) Four-terminal resistance  $R_{51,i6}$  for current flowing between  $5 \leftarrow 1$  and voltage drop across  $i - 6$  for  $i \in \{2, 3, 4\}$  corresponding to  $\ell = \{0.7, 2.9, 5\}$   $\mu\text{m}$  between the three panels for a set of four magnetic field settings on the  $\nu = 4$  plateau. (e)-(g) Similar to (b)-(d), but for three magnetic field settings on the  $\nu = 3$  plateau.

a higher time constant of 100 ms, corresponding to a 3 decibel bandwidth of  $f_{3dB} = 2.4$  Hz. We wait  $t_s = 350$  ms between single-shot measurements for the lock-in to settle, corresponding to a sampling frequency  $f_s$  of roughly 3 Hz.

One key consistency check for ensuring that measured current noise from the Coulomb flank method is genuine charge noise coming from the device is to measure the current noise both while a) sitting in the valley between Coulomb blockade peaks and while b) sitting on a Coulomb blockade peak. These measurements are done in addition to the noise measurements on the flank of a Coulomb blockade peak, as described in the main text. For genuine charge noise, the measured noise on the flanks should be significantly higher than the noise on the peak or in the valley, given that charge noise induces fluctuations in the quantum dot's local electrochemical potential. We compare the flank data from the main text to measurements from the valley in between Coulomb peaks and from the maxima of the Coulomb peaks themselves, in figure S4. The higher measured noise spectrum for the flanks indicates that the noise is indeed higher than the setup noise floor and is a clear signature of charge noise.

Having established that we are measuring charge noise intrinsic to the device, we collect 14 different time-series measurements of the noise using the Coulomb flank method. These 14 traces are converted to power spectral densities of the electrochemical potential using equation 5, and are plotted in figure S5. Averaging the measured noise at 1 Hz present in these 14 traces gives our estimated  $S_\mu(1\text{Hz}) = 0.45 \mu\text{eV}^2/\text{Hz}$ .

The second method that we use to measure charge noise is Coulomb peak tracking, where we repeatedly sweep along a Coulomb peak over time. The time series data of the peak location can be directly converted to a plunger gate voltage noise, which can be converted to an energy scale using the lever arm  $\alpha$ .

## S7. SENSITIVITY OF THE CONDUCTANCE TO PLUNGER AND QUANTUM POINT CONTACT GATE VOLTAGES

In this section, we justify the assumption made in Sec.IV A of neglecting contributions from fluctuations in the QPC gate voltage  $V_{\text{qpc}}$  when evaluating the RMS charge noise in Eq.6 of the main text. Figure S6 presents data from Device C, measured during a separate cooldown, comparing the sensitivity of the hybrid dot conductance to  $V_{\text{qpc}}$  and to the plunger gate voltage  $V_{\text{pr}}$ .

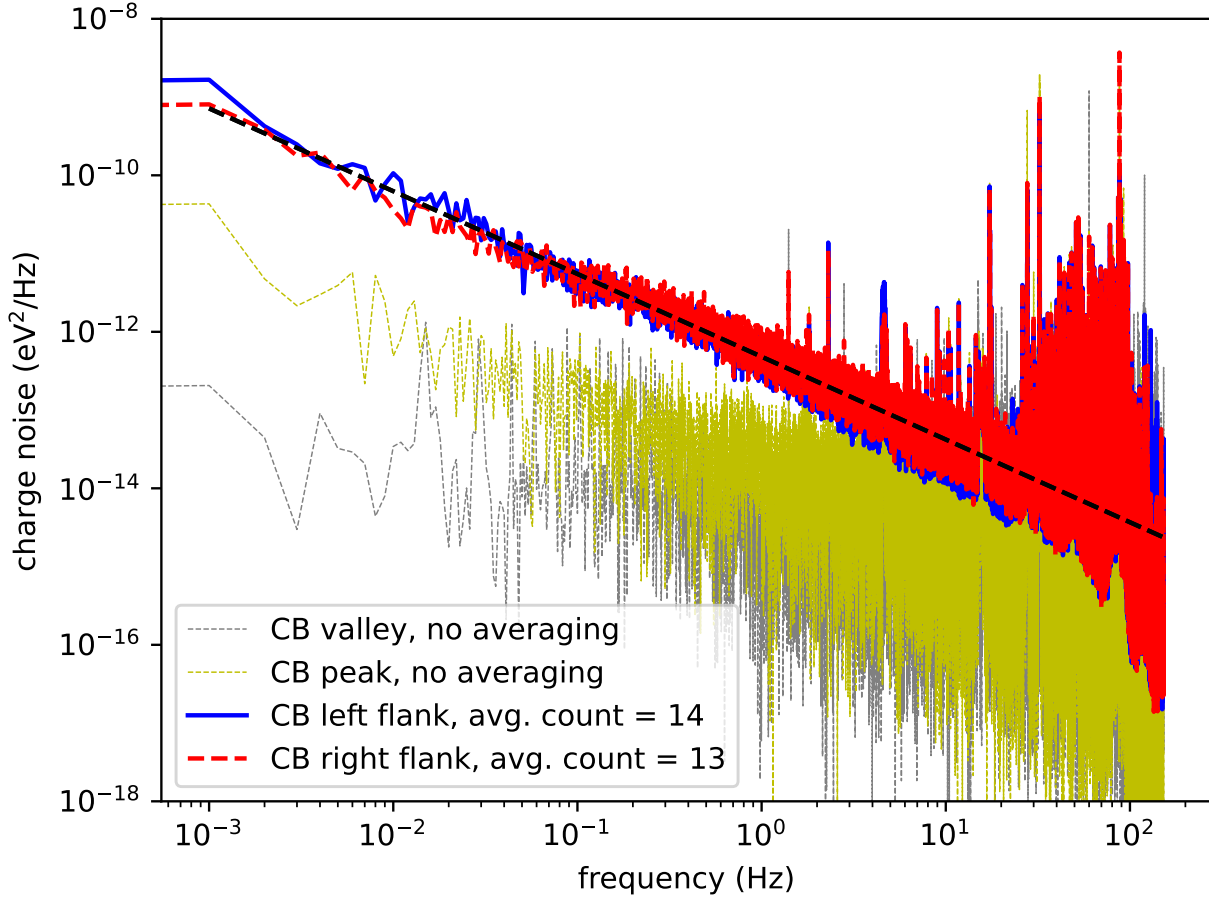


FIG. S4. Power spectral density curves for time series data taken on the left (blue) and right (red) flanks of a Coulomb blockade peak, as well exactly at the peak position (yellow), and in the valley (gray). The valley and peak noise spectra are not averaged, whereas the Coulomb flank spectra are averaged over the 14 and 13 measured traces for left and right flanks, respectively.

A thermally broadened Coulomb peak in the weak tunneling limit is shown in Fig.S6(c), with the transconductance peaking on the Coulomb peak flank, analogous to Fig.4(b) in the main text.

To assess the effect of small changes in  $V_{\text{qpc}}$ , we measured a series of Coulomb peaks as a function of  $V_{pR}$ , shown in Fig.S6(a). Each trace corresponds to a different value of  $V_{\text{qpc}}$  applied uniformly to all QPC gates, spanning the range  $[-3.62, -3.636]$  V in 0.5 mV steps. Due to cross-capacitance between the QPC and plunger gates, the peak positions shift, so we track the peak conductance—defined at  $\delta V_{pR} = 0$ —as a function of  $V_{\text{qpc}}$  in Fig.S6(b).

The peak conductance values in Fig.S6(b) are extracted by fitting the annotated Coulomb peaks in Fig.S6(a) to Eq.3. As expected,  $G_{\text{peak}}$  decreases as the QPC transmissions  $\tau_{1,2}$  are suppressed by more negative  $V_{\text{qpc}}$ . The slope of this decrease is relatively small, with  $|dG_{\text{peak}}/dV_{\text{qpc}}| < 3 e^2/hV$ , representing over a 100-fold weaker sensitivity to  $V_{\text{qpc}}$  compared to the plunger gate. This is evident in Fig.S6(c), where the transconductance  $dG/dV_{pR}$  is more than two orders of magnitude larger than the sensitivity to  $V_{\text{qpc}}$ .

These observations justify neglecting the effect of QPC voltage fluctuations when estimating hybrid dot charge noise.

### S8. CHARGE NOISE CONTRIBUTION TO COULOMB PEAK WIDTH

In the thermally broadened, weak-coupling limit, the Coulomb peak lineshape is described by Eq. 3:

$$G(x) = G_0 \frac{x}{\sinh(x)}, \quad (\text{S21})$$

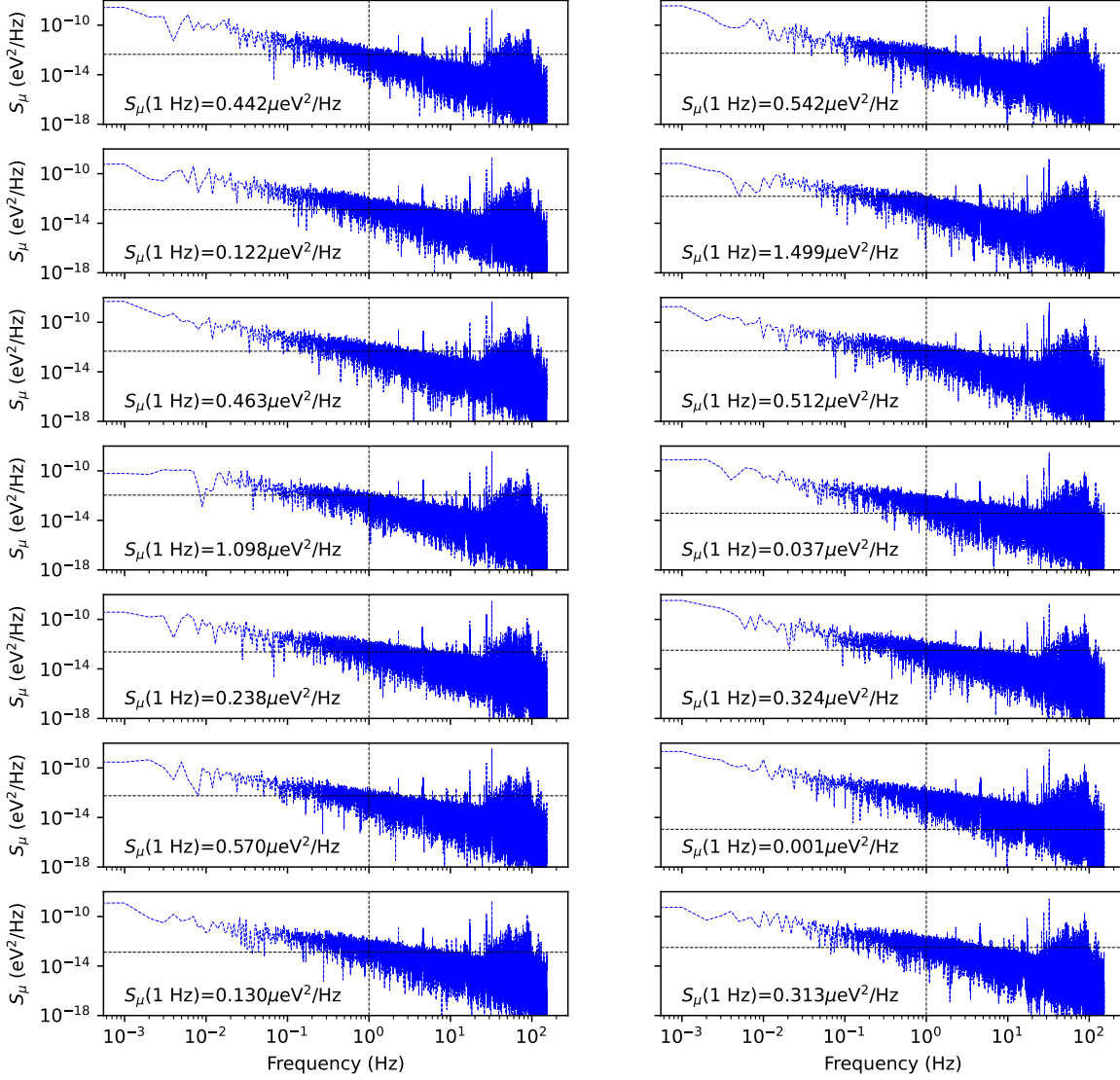


FIG. S5. For the Coulomb flank method shown in the main text, the power spectral density curves for each of the 14 peaks that we tracked are plotted, along with a text inset presenting the measured value of the charge noise at 1 Hz, (shown at the intersection of the dashed black lines). Averaging these numbers yields  $S_\mu(1 \text{ Hz}) = 0.45 \pm 0.11 \mu\text{eV}^2/\text{Hz}$ .

where  $x = \alpha\delta V_{pR}/k_B T_e$ . The full width at half maximum (FWHM) of this lineshape in the absence of charge noise is given by:

$$x_{\text{FWHM}}(\sigma_\mu = 0) = 4.354. \quad (\text{S22})$$

Since  $\alpha\delta V_{pR}$  corresponds to the electrochemical potential  $\mu$ , we incorporate the effect of charge noise by treating  $x$  as a normally distributed random variable:  $X \sim \mathcal{N}(x_0, \sigma_x)$ , where  $x_0 = \alpha\delta V_{pR,0}/k_B T_e$  corresponds to the gate-tunable mean electrochemical potential  $\mu_0 = \alpha\delta V_{pR,0}$ , and  $\sigma_x = \sigma_\mu/k_B T_e = 0.47$ , based on Eq. 6.



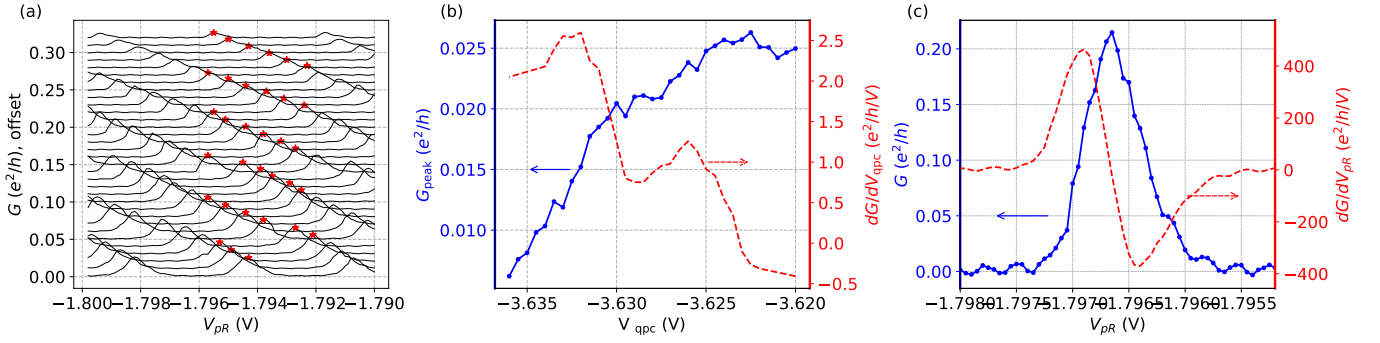


FIG. S6. (a) Device C hybrid dot conductance as a function of the plunger gate voltage  $V_{PR}$ . Each trace in (a) corresponds to a fixed voltage  $V_{qpc} \in [-3.62, -3.636]$  V with a step size of 0.5 mV applied to all the QPC gates. The second conductance peak in each trace is annotated with a red-star. The offset in peak positions is a result of the cross-capacitance between the QPC and the plunger gates. The traces are offset vertically for clarity. (b) The conductance of the second peak for each trace in (a) is plotted as a function of  $V_{qpc}$  (blue), showing an overall decrease in peak  $G_{peak}$  conductance as the transmissions  $\tau_{1,2}$  are reduced with  $V_{qpc}$ . The red dashed curve shows the slope  $dG_{peak}/dV_{qpc}$ . (c) Coulomb peak (blue) for  $V_{qpc} = -3.636$  V and transconductance (red) as a function of plunger gate voltage  $V_{PR}$ . As discussed in the main text, the plunger gate is tuned to the flank for CPF measurements, where  $dG/dV_{PR}$  over 100 times larger than the maximum sensitivity to  $dG_{peak}/V_{qpc}$ .

The expected peak conductance at  $x_0 = 0$  is then given by:

$$\mathbb{E} \left[ G_0 \frac{X}{\sinh X} \right] = G_0 \int_{-\infty}^{\infty} \frac{x}{\sinh x} \frac{1}{\sqrt{2\pi\sigma_x^2}} e^{-\frac{x^2}{2\sigma_x^2}} dx = 0.965 G_0. \quad (S23)$$

To evaluate the Coulomb peak FWHM in the presence of charge noise, we find the mean offset  $X = x^*$  such that  $\mathbb{E}[G(X)] = 0.4825 G_0$ :

$$\mathbb{E} \left[ G_0 \frac{X}{\sinh X} \right] = G_0 \int_{-\infty}^{\infty} \frac{x}{\sinh x} \frac{1}{\sqrt{2\pi\sigma_x^2}} e^{-\frac{(x-x^*)^2}{2\sigma_x^2}} dx = 0.4825 G_0, \quad (S24)$$

which can be solved numerically, yielding  $x^* = 4.412$ . This gives:

$$x_{FWHM}(\sigma_\mu = 2.2 \mu\text{eV}) = 4.412. \quad (S25)$$

Equations S23 and S25 thus reveal a modest 1.5% increase in Coulomb peak FWHM due to electrochemical potential fluctuations.

## S9. HYBRID DOT CHARGE QUANTIZATION IN THE NEARLY BALLISTIC LIMIT

In the quantum near-ballistic limit ( $k_B T \ll E_c, 1 - \tau_{1,2} \ll 1$ ), the theory of strong inelastic cotunneling predicts a conductance

$$G = \frac{e^2}{2h} \left[ 1 - \int_0^\infty \frac{\Gamma_-^2 / \cosh^2 x}{(x\pi^2 k_B T / \gamma E_c)^2 + \Gamma_-^2} dx \right], \quad (S26)$$

where  $\gamma \approx \exp(0.5772)$ , and

$$\Gamma_- = (1 - \tau_1) + (1 - \tau_2) - 2\sqrt{(1 - \tau_1)(1 - \tau_2)} \cos(2\pi\delta V_g / \Delta) \quad (S27)$$

Predictions of the visibility of conductance oscillations,  $Q$ , based on Eq. S26 for  $1 - \tau_{1,2} < 0.01$  are shown as solid curves in Fig. 5(b) in the main text. In proximity to the ballistic critical point for one of the QPCs,  $\sqrt{1 - \tau_2} \ll 1$ , the visibility  $Q$  is well described by the asymptotic  $\sqrt{1 - \tau_2}$  scaling relation,

$$G = \frac{\gamma}{\pi} \frac{E_c}{k_B T} \sqrt{(1 - \tau_1)(1 - \tau_2)}, \quad (S28)$$

as shown by the dashed curves in Fig. 5(b) in the main text. Focusing on the scaling dependence on the independent parameter  $\tau_2$  for a fixed voltage on the bottom QPC, we leave  $\tau_1$  as a fit parameter to account for the drift in bottom QPC transmission over the course of  $G(V_{PR})$  measurements.

### S10. DYNAMICAL COULOMB BLOCKADE FRAMEWORK

In this section, we review the expressions for conductance suppression of a short conductor in the weak tunneling limit ( $\tau \ll 1$ ) embedded in a resistive environment, as calculated by Joyez and Esteve.

Considering the environment impedance  $Z$ , temperature  $T$ , and bias voltage  $V$ , the differential conductance  $G = dI/dV$  through the short conductor is given by

$$G(V) = \frac{1 + E_B(Z, V, T)}{R_T}, \quad (\text{S29})$$

$$= \frac{1}{R_T} \left[ 1 + 2 \int_0^\infty \pi t \left( \frac{k_B T}{\hbar} \right)^2 \times \Im[\exp J(t)] \cos \frac{eVt}{\hbar} \sinh^{-2} \frac{\pi t k_B T}{\hbar} dt \right], \quad (\text{S30})$$

where  $R_T = 1/G_\infty$  is the intrinsic tunnel resistance, taken to be much larger than the environment resistance in this framework  $\Re[Z] = R_{\text{env}} \ll R_T$ .

Modeling the environment as an  $RC$  circuit with  $R_{\text{env}} = \frac{\hbar}{e^2 \tau_2}$  set by the top QPC transmission and  $C = e^2/2E_c$  determined by the hybrid dot charging energy,  $J(t)$  is given by

$$J(t) = \frac{\pi R}{R_K} \left( \left( 1 - e^{-|t|/R_{\text{env}} C} \right) \left( \cot \frac{\hbar}{2RCk_B T} - i \right) - \frac{2k_B T |t|}{\hbar} + 2 \sum_{n=1}^\infty \frac{1 - e^{-\omega_n |t|}}{2\pi n [(RC\omega_n)^2 - 1]} \right), \quad (\text{S31})$$

where  $\omega_n = \frac{2\pi n k_B T}{\hbar}$  are the Matsubara frequencies for  $n \in \mathbb{Z}^+$ , and

$$2 \sum_{n=1}^\infty \frac{1 - e^{-\omega_n |t|}}{2\pi n [(RC\omega_n)^2 - 1]} = -\frac{1}{\pi} \left[ 2\gamma + \Psi(-x) + \Psi(x) + 2\ln(1-y) + \frac{y}{1+x} {}_2F_1(1, 1+x, 2+x, y) + \frac{y}{1-x} {}_2F_1(1, 1-x, 2-x, y) \right], \quad (\text{S32})$$

where  $\gamma$  is Euler's constant,  $\Psi$  is the logarithmic derivative of the Gamma function,  ${}_2F_1$  is the hypergeometric function,  $y = \exp\left(\frac{-2\pi t k_B T}{\hbar}\right)$ , and  $x = \frac{\hbar}{e^2} \frac{E_c}{4\pi^2 R_{\text{env}} k_B T}$ .

### S11. COULOMB DIAMOND AND ELECTRON THERMOMETRY DATA FOR DEVICE C

A larger hybrid quantum dot (Device C) fabricated on a different  $5 \times 5 \text{ mm}^2$  chip was tuned for studying dynamical Coulomb blockade (see Fig.S S7(a)). With the 2DEG tuned to low filling factor quantum Hall, the formation of unintentional quantum dots in a quantum point contact presents a fundamental challenge in realizing smooth and monotonic control of edge mode transmissions. These quantum dots may result from a combination of edge mode reconstruction in a smooth confining potential and disorder-induced density modulation in the incompressible region in the QPC. A QPC design robust to the formation of quantum dots will be addressed in a future work. Although the QPCs in Devices B, and C were nominally identical, the unintentional quantum dots in Device C, if any, were weakly coupled to the edge modes resulting in smooth and monotonic tunability over the entire range shown in Fig. 6(d) in the main text. Consequently, Device C presented an attractive playground for a quantitative study of the low bias  $eV_{dc} \ll E_c$  suppression of transmission in a resistive environment.

Data for extracting the charging energy  $E_c = 70 \text{ } \mu\text{eV}$  for Device C and the electron temperature  $T = 59 \pm 2 \text{ mK}$  for the corresponding cooldown is shown in Fig. S7.

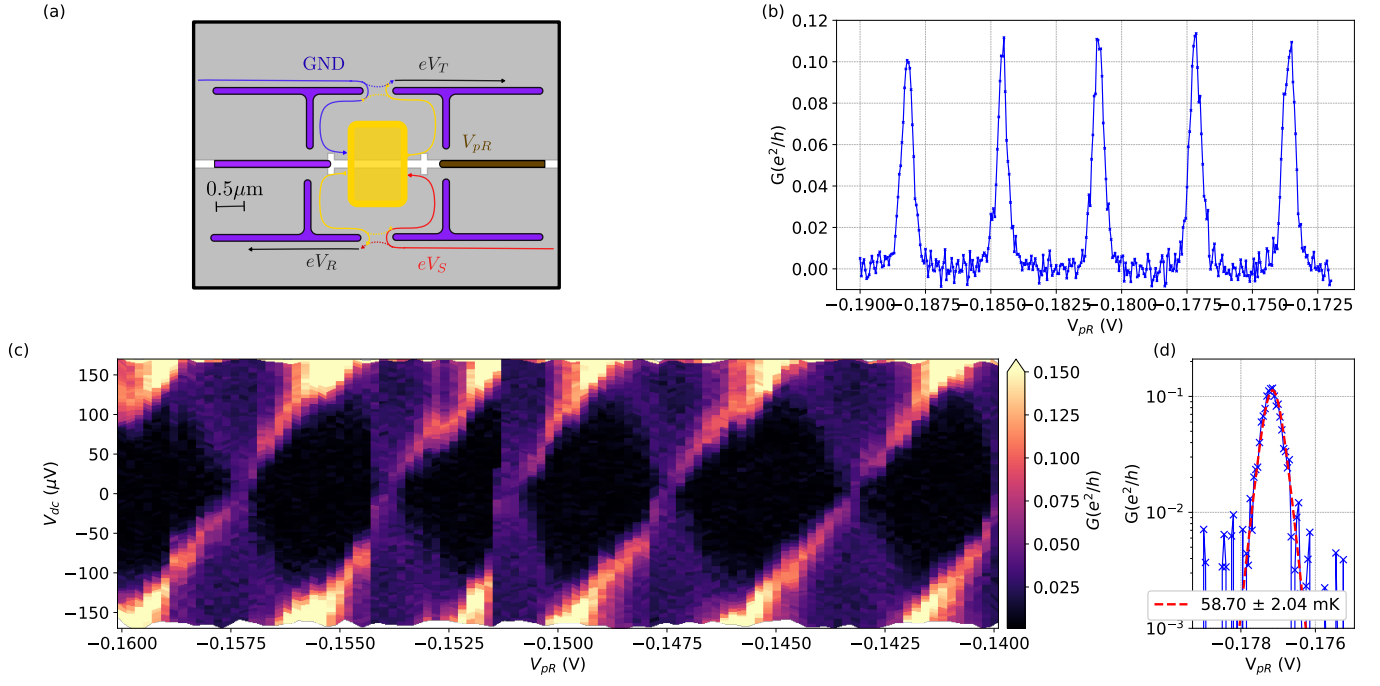


**FIG. S7. Device C Static Coulomb blockade.** (a) Schematic of the hybrid metal-semiconductor quantum dot (Device C). A rectangular Ti/Au island with a  $0.8 \times 1.2 \mu\text{m}^2$  footprint makes sidewall contact to the InAs quantum well across a  $120 \text{ nm}$  wide trench (white) on a mesa (gray). The QPC and plunger gates (purple, red) are biased with dc voltage sources, and the right plunger (red) is swept to reveal Coulomb blockade oscillations. The device is biased with a  $500 \text{ pA}$  low-frequency ( $< 30 \text{ Hz}$ ) ac excitation and a dc current bias  $i_{dc}$ . A pair of contacts on either end are tied to ground at the mixing chamber stage of the dilution fridge, and realize a “cold” ground to drain current. The source ( $V_S$ ), reflected ( $V_R$ ), and transmitted ( $V_T$ ) voltage drops to ground are measured  $\sim 45\text{-}\mu\text{m}$  from the island after amplification by lock-in amplifiers. (b) Coulomb blockade oscillations in the series conductance  $G$  as a function of the plunger gate voltage  $V_{pR}$  for a set of 5 successive charging events, with the QPCs tuned to the weak tunneling limit  $\tau_{1,2} \ll 1$ . (c) Coulomb diamonds measured by a dc current  $|I_{dc}| < 20 \text{ nA}$ . The source dc voltage drop  $V_{dc} = I_{dc} \times h/3e^2$  is measured using a multimeter. The charging energy estimated from the diamond heights  $E_c = e^2/2C = 70 \mu\text{eV}$ , where  $C$  is the capacitance of the hybrid dot. (d) A Coulomb peak from (a) on a semi-log scale fit to Eq. 3 for determining the electron temperature =  $59 \text{ mK}$ .